Neuron

Article

Sparse Activity of Hippocampal Adult-Born Neurons during REM Sleep Is Necessary for Memory Consolidation

Graphical Abstract

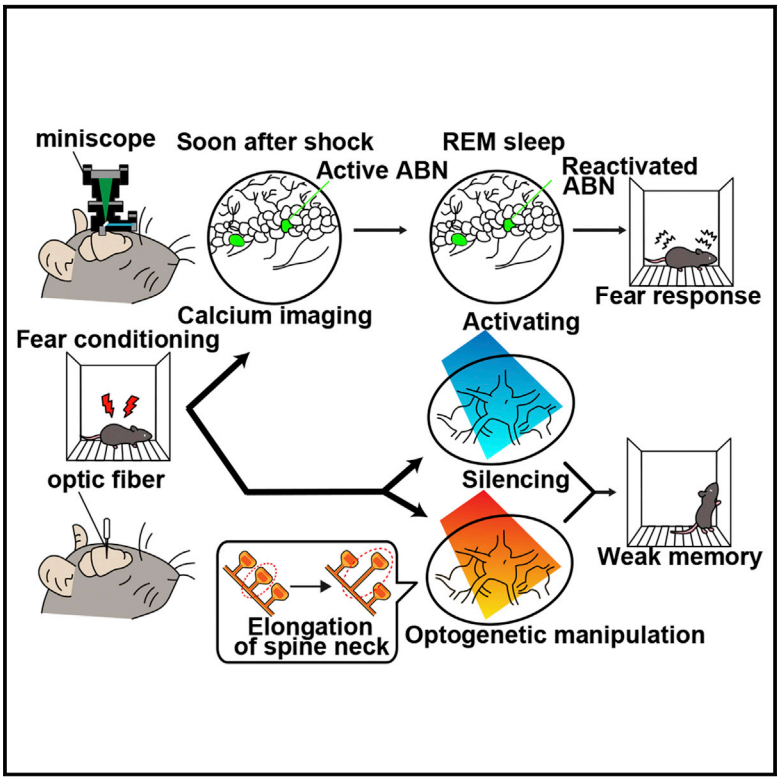

Highlights

- Adult-born neuron (ABN) activity during sleep can be seen using Ca^{2+} imaging
- ABNs active after learning reactivate in subsequent rapid eye movement (REM) sleep
- Optogenetic manipulation of ABN activity in REM sleep impairs memory consolidation
- This effect may be mediated by ABN synaptic plasticity

Authors

Deependra Kumar, Iyo Koyanagi, Alvaro Carrier-Ruiz, ..., Masanobu Kano, Masashi Yanagisawa, Masanori Sakaguchi

Correspondence

sakaguchi.masa.fp@alumni.tsukuba.ac.jp

In Brief

The neuronal population in the hippocampus responsible for memory consolidation during rapid eye movement (REM) sleep was unknown. Using *in vivo* imaging and optogenetics, Kumar et al. provide causal evidence that the activity of dentate gyrus adult-born neurons during REM sleep is necessary for contextual fear memory consolidation.

Kumar et al., 2020, Neuron *107*, 552–565
August 5, 2020
https://doi.org/10.1016/j.neuron.2020.05.008

CellPress

CellPress

Neuron

Article

Sparse Activity of Hippocampal Adult-Born Neurons during REM Sleep Is Necessary for Memory Consolidation

Deependra Kumar,[1] Iyo Koyanagi,[1,12] Alvaro Carrier-Ruiz,[2,3,12] Pablo Vergara,[1,12] Sakthivel Srinivasan,[1,12] Yuki Sugaya,[2,3] Masatoshi Kasuya,[1] Tzong-Shiue Yu,[4] Kaspar E. Vogt,[1] Masafumi Muratani,[5] Takaaki Ohnishi,[6] Sima Singh,[1] Catia M. Teixeira,[7] Yoan Chérasse,[1] Toshie Naoi,[1] Szu-Han Wang,[8] Pimpimon Nondhalee,[1] Boran A.H. Osman,[1] Naoko Kaneko,[9] Kazunobu Sawamoto,[9,10] Steven G. Kernie,[4] Takeshi Sakurai,[1] Thomas J. McHugh,[11] Masanobu Kano,[2,3] Masashi Yanagisawa,[1] and Masanori Sakaguchi[1,13,*]

[1]International Institute for Integrative Sleep Medicine (WPI-IIIS), University of Tsukuba, Tsukuba, Ibaraki 305-0006, Japan

[2]Department of Neurophysiology, Graduate School of Medicine, The University of Tokyo, Tokyo 113-0033, Japan

[3]International Research Center for Neurointelligence (WPI-IRCN), The University of Tokyo Institutes for Advanced Study (UTIAS), Tokyo 113-0033, Japan

[4]Department of Pediatrics, Columbia University College of Physicians and Surgeons, New York, NY 10032, USA

[5]Department of Genome Biology, Faculty of Medicine, University of Tsukuba, Tsukuba, Ibaraki 305-0006, Japan

[6]Graduate School of Information Science and Technology, The University of Tokyo, Tokyo 113-8656, Japan

[7]Emotional Brain Institute, Nathan Kline Institute, Orangeburg, NY 10962, USA

[8]Centre for Clinical Brain Sciences, Centre for Cognitive Ageing and Cognitive Epidemiology, University of Edinburgh, Edinburgh EH16 4SB, UK

[9]Department of Developmental and Regenerative Biology, Institute of Brain Science, Nagoya City University Graduate School of Medical Sciences, Nagoya, Aichi 467-8601, Japan

[10]Division of Neural Development and Regeneration, National Institute for Physiological Sciences, Okazaki, Aichi 444-8585, Japan

[11]RIKEN Center for Brain Science, Wako, Saitama 351-0106, Japan

[12]These authors contributed equally

[13]Lead Contact

*Correspondence: sakaguchi.masa.fp@alumni.tsukuba.ac.jp

https://doi.org/10.1016/j.neuron.2020.05.008

SUMMARY

The occurrence of dreaming during rapid eye movement (REM) sleep prompts interest in the role of REM sleep in hippocampal-dependent episodic memory. Within the mammalian hippocampus, the dentate gyrus (DG) has the unique characteristic of exhibiting neurogenesis persisting into adulthood. Despite their small numbers and sparse activity, adult-born neurons (ABNs) in the DG play critical roles in memory; however, their memory function during sleep is unknown. Here, we investigate whether young ABN activity contributes to memory consolidation during sleep using Ca^{2+} imaging in freely moving mice. We found that contextual fear learning recruits a population of young ABNs that are reactivated during subsequent REM sleep against a backdrop of overall reduced ABN activity. Optogenetic silencing of this sparse ABN activity during REM sleep alters the structural remodeling of spines on ABN dendrites and impairs memory consolidation. These findings provide a causal link between ABN activity during REM sleep and memory consolidation.

INTRODUCTION

The capacity to recall specific experiences, known as episodic memory, depends on the hippocampus (Vargha-Khadem et al., 1997). Rodents may hold a primitive version of an episodic memory system in the hippocampus (Allen and Fortin, 2013; Dere et al., 2005). This brain structure is unique in that its dentate gyrus (DG) exhibits neurogenesis that persists across the lifespan in mammals, including humans (Altman and Das, 1965; Boldrini et al., 2018; Eriksson et al., 1998; Moreno-Jiménez et al., 2019; but see Sorrells et al., 2018). Despite their scarcity (Imayoshi et al., 2008) and infrequent activity (Danielson et al., 2016), DG adult-born neurons (ABNs) provide a distinctive form of plasticity to the brain and may play an essential role in survival (Kempermann, 2012). In particular, young ABNs show enhanced synaptic plasticity compared with their fully mature counterparts and hence may be preferentially recruited into memory traces (Ge et al., 2007; Gu et al., 2012; Kee et al., 2007; Marín-Burgin et al., 2012; Park et al., 2016). Indeed, the amount of adult neurogenesis correlates with the strength and persistence of memories (Akers et al., 2014; Alam et al., 2018; Clelland et al., 2009; Kitamura et al., 2009; Nakashiba et al., 2012; Sahay et al., 2011; Shors et al., 2001).

Temporally specific optogenetic silencing of ABN activity reveals the necessity of young ABNs in learning and memory retrieval (Danielson et al., 2016; Gu et al., 2012; Huckleberry et al., 2018; Zhuo et al., 2016). So far, to our knowledge, only one study has optogenetically increased and decreased the activity of young ABNs *in vivo* to examine their role in memory (Danielson et al., 2016). Interestingly, both manipulations impaired memory (Danielson et al., 2016), suggesting that young ABN activity is finely tuned in concert with ongoing neural activity (Luna et al., 2019) during memory consolidation. However, efforts to analyze the activity of ABNs have been hampered by their small numbers and infrequent activity. The only previous study examining real-time ABN activity using Ca^{2+} imaging in awake, head-fixed mice limited the recording session to a maximum of 12 min, which is insufficient to capture rare events across the sleep-wake cycle. Although this study confirmed that ABNs are capable of encoding contextual information (Danielson et al., 2016), the contribution of ABN activity to memory consolidation during sleep remains unexplored.

In mammals, sleep occurs in cycles of rapid eye movement (REM) and non-REM (NREM) sleep. Each sleep stage is characterized by local and global synchronous neuronal activities that play critical roles in memory consolidation. For example, during NREM sleep, boosting slow oscillations enhances memory (Marshall et al., 2006), whereas silencing synchronous activity across cortical regions (Miyamoto et al., 2016) or disrupting sharp-wave ripples in the hippocampus (Girardeau et al., 2009) impairs memory consolidation. Similarly, in REM sleep, disrupting theta rhythm, the dominant oscillatory pattern in the hippocampus, impairs long-term memory storage (Boyce et al., 2016). These synchronous activities may affect memory consolidation by enabling the reorganization of synapses that were formed or underwent plasticity during wakefulness (Norimoto et al., 2018; Yang et al., 2014). Indeed, the timing of neuronal activity in relation to local DG theta oscillations plays a critical role in synaptic strength (Orr et al., 2001). Another line of evidence shows that hippocampal ensemble activities during wakefulness are replayed during subsequent sleep (Ghandour et al., 2019; Louie and Wilson, 2001; Wilson and McNaughton, 1994), which may enhance memory consolidation. Currently, however, the specific types of hippocampal cells that enable memory consolidation during REM sleep are not known, warranting studies that clarify the function of ABNs in memory consolidation during sleep.

RESULTS

Young ABN Activity Decreases in REM Sleep during Contextual Fear Memory Consolidation

To target ABNs, we used a pNestinCreER^{T2} (nestin) mouse line (Lagace et al., 2007) for which targeting specificity was confirmed by previous studies (Gao et al., 2009; Guo et al., 2011; Knobloch et al., 2013; Ninkovic et al., 2013). Crossing nestin mice with Rosa-pCAG-LSL-tdTomato reporter mice generated offspring (tdTomato^{nestin}) in which we confirmed maturation-specific marker expression in labeled neurons upon tamoxifen injection (Figure S1), replicating previous results (Lagace et al., 2007). To examine ABN activity during sleep, we employed Ca^{2+} imaging under freely moving conditions using miniaturized microendoscopes (Ghosh et al., 2011) (Figure 1A). Crossing nestin mice with Rosa-pCAG-LSL-GCaMP3 (GC) mice generated offspring (GC^{nestin} mice; Figure 1B) in which 4-week-old and younger ABNs (hereafter, young ABNs) express the Ca^{2+}-dependent fluorescence reporter GCaMP3 (Tian et al., 2009) (Figures 1B and 1C; Figure S1H). At this point in development, young ABNs are integrated into medial temporal lobe neuronal circuitry (Figure S2). Consistent with the reported ABN Ca^{2+} event rate during wakefulness (Danielson et al., 2016), we found that young ABNs showed sparse activity during wakefulness, with even less frequent activity during NREM and REM sleep (Figure 1D; Figures S3 and S4A–S4G; Videos S1 and S2).

To examine young ABN activity across sleep-wake states during memory consolidation, we employed a single-trial hippocampus-dependent contextual fear conditioning paradigm that requires the activity of young ABNs for learning and memory retrieval (Danielson et al., 2016; Gu et al., 2012). Microendoscope-implanted GC^{nestin} mice were randomly assigned to two groups. Mice in the immediate shock (IS) control group received foot shocks immediately upon context entry, whereas mice in the delayed shock (DS) group received foot shocks after exploring the context (Figure 1E). The only difference between groups was shock timing, because shock number and intensity and the duration of context exposure were identical. 24 h later, mice in the DS group showed a pronounced freezing response upon context re-exposure, whereas mice in the IS group did not (Figure 1F). This low freezing in the IS group is considered to reflect a weak shock-context association when shock is delivered shortly after context exposure (Blanchard et al., 1976; Fanselow, 1986; McHugh and Tonegawa, 2007). Consistent with our earlier observation (Figure 1D), Ca^{2+} transient probability was lower in NREM and REM sleep than in wakefulness for both groups (Figures 1G and 1H). However, after contextual fear conditioning, Ca^{2+} transient probability in REM sleep was further reduced in the DS group, but not in the IS group, with no change in sleep architecture (Figures 1G and 1H; Figures S4H–S4R). This activity reduction during REM sleep was not observed when we examined fully mature DG granule neurons from GC mice injected with AAV:pCaMKII-Cre (Stefanelli et al., 2016) instead of nestin mice (Figures S5A–S5C; average labeled cell density, 33 ± 8.7 per μm^2). These results suggest that consolidation of the context-shock association, but not of context or shock representations alone, reduces young ABN activity in REM sleep.

Contextual Fear Learning Recruits a Young ABN Population That Is Reactivated during REM Sleep

To better characterize the reduction in young ABN activity in REM sleep during memory consolidation, we longitudinally followed the activity of individual ABNs across learning, consolidation, and retrieval. In addition to recording ABN activity during sleep, we recorded activity during four awake periods: (1) home cage (HC) immediately before conditioning (10 min, pre-shock HC), (2) pre-shock during conditioning in context A (10 min, pre-shock A), (3) post-shock during conditioning (5 min, post-shock A), and (4) memory retrieval test (10 min; test A) (Figure 1I). Because it was challenging to track the

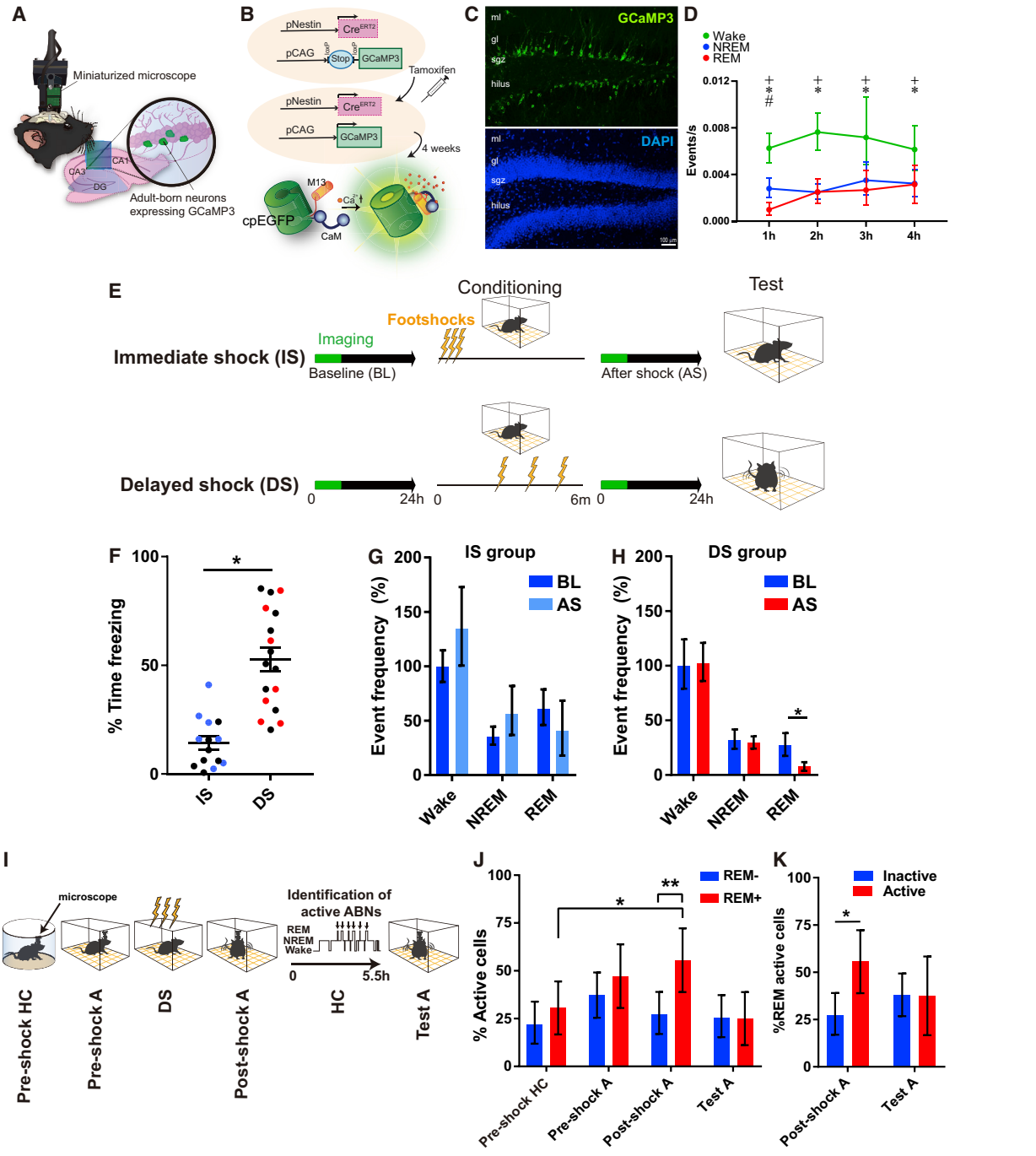

Figure 1. Young ABN Activity Decreases in REM Sleep during Contextual Fear Memory Consolidation

(A) Ca^{2+} imaging.

(B) Transgenic method.

(C) GCaMP expression.

(D) Ca^{2+} event frequency ($^{+}$NREM versus wake, *wake versus REM, $^{\#}$REM versus NREM, $p < 0.05$, bootstrap; error bars, 95% confidence interval [CI]; n = 46 neurons from 4 mice).

(E) Contextual fear conditioning. Ca^{2+} imaging was performed after shock (AS) and during a circadian time-matched baseline (BL) period.

(F) Freezing by IS and DS mice upon context re-exposure (n = 14 and 17 mice in IS and DS groups, respectively; *$p < 0.0001$, two-tailed unpaired t test with Welch's correction; error bars, SEM). Mice indicated by blue and red markers were used for further Ca^{2+} imaging analysis.

(G and H) Ca^{2+} event frequency in sleep-wake states in IS (G) and DS (H) group (*$p < 0.05$, bootstrap; error bars, 95% CI; n = 88, 47, 113, and 137 neurons in IS-BL, IS-AS, DS-BL, and DS-AS groups, respectively).

(legend continued on next page)

same ABNs over time due to their sparse activity against slight but consistent changes in the field of view, we shortened the duration (5.5 h) between conditioning and testing to minimize field of view changes. This duration covers the period during which memory is protein synthesis dependent (Bourtchouladze et al., 1998). These changes in experimental conditions resulted in overall low freezing during the test, but freezing remained specific to the shocked context (Figure S4S).

We first sorted ABNs into two groups based on the presence (REM+) or absence (REM−) of their activity during post-learning REM sleep and examined their activity during learning and retrieval. REM+ ABNs were defined as being active at least once during any REM episode, which represented 37.9% (±5.0% SEM) of all recorded ABNs. Interestingly, REM+ ABNs were more likely to be active during the post-shock period than during the HC period or compared with REM− ABNs (Figure 1J). Although one could assume that REM+ ABNs would be reactivated during the memory retrieval test if they encoded the memory trace, there was no difference in the likelihood of REM+ versus REM− ABNs being active during the test (Figure 1J), suggesting that REM+ ABNs participate during learning more than during memory retrieval. Considering these results, we next sorted ABNs based on their activity or inactivity during learning and retrieval and compared their activity during REM sleep. ABNs that were active in the post-shock period were more likely to be active during subsequent REM sleep (Figure 1K). By contrast, ABNs that were active or inactive during the memory retrieval test showed no difference in their likelihood of being active during REM sleep. REM+ and REM− ABNs had chance levels of being active during both the post-shock and test periods (Figure S4T). Ca^{2+} event frequency was similar between REM+ and REM− ABNs across the four periods (Figure S4U). Overall, these results suggest that most of the young ABNs that are active during post-learning REM sleep are those that were active during learning.

Silencing Young ABN Activity in REM Sleep Does Not Affect Sleep or DG Theta Oscillations

Based on these results, we hypothesized that the sparse activity of young ABNs during REM sleep contributes to memory consolidation. Because the fine-tuning of this activity may be critical for memory consolidation, we performed optogenetic silencing to reveal its function (Danielson et al., 2016; Gu et al., 2012; Huckleberry et al., 2018; Zhuo et al., 2016). Crossing nestin mice with Rosa-pCAG-LSL-halorhodopsin (Halo) mice generated offspring ($Halo^{nestin}$). We induced expression of Halo in young ABNs by tamoxifen injection in $Halo^{nestin}$ mice (Figure 2A) to allow their silencing in a temporally specific and reversible manner upon delivery of orange light (Zhang et al., 2007). As expected, Cre-negative littermate $Halo^{WT}$ mice did not express Halo upon tamoxifen injection (Figure 2B). We next confirmed the temporal specificity and reversibility of silencing young ABN action potentials. To overcome the sparseness of ABN activity, we activated young ABNs by current injection in acute brain slices of $Halo^{nestin}$ mice (Figure 2C) and observed a transient silencing of action potentials in response to orange light delivery with high temporal fidelity and reversibility (Figures 2D–2F).

We next examined whether the silencing of activity during REM sleep after contextual fear conditioning affects sleep architecture. $Halo^{nestin}$ and $Halo^{WT}$ mice underwent DS conditioning followed by optogenetic silencing selectively during REM sleep by monitoring electroencephalogram (EEG) activity in real time for 6 h (Figures 3A and 3B; Table S1). We estimate that a minimum of 467 ABN Ca^{2+} events per mouse were affected by optogenetic silencing during this period (although there are differences in focal planes and observation points between imaging and optogenetic manipulation experiments; Figure 3C). This estimation is based on our knowledge that: (1) there are an average of 198 ABNs in the DG upper blade in a 40-μm section (Figure S1D), (2) the light-effective length along the AP axis is 450 μm (Figure 3C), (3) the average REM duration in the optogenetic intervention period was 22.2 min (Halo-AS; Figure 3D), (4) light was delivered for 50% of the targeted sleep stage, and (5) there were an average of 0.0189 Ca^{2+} events/min during REM sleep in the DS-AS group; therefore, $198 \times (450\ \mu m/40\ \mu m) \times 22.2 \times 0.5 \times 0.0189 = 467$. We observed that optogenetic silencing did not alter sleep architecture or EEG power spectra (Figures 3D–3F).

Hippocampal theta oscillations during REM sleep influence neuronal activity in a manner that allows memory consolidation (Boyce et al., 2016), and DG theta oscillations play a critical role in spike-timing-dependent synaptic plasticity (Orr et al., 2001). Moreover, reactivation of awake CA1 ensemble activity during subsequent REM sleep may affect local theta oscillations (Louie and Wilson, 2001). To examine whether young ABN activity during REM sleep affects DG theta oscillations, we recorded local field potentials (LFPs) in the DG while silencing ABNs during REM sleep during the memory consolidation period (Figure 3I). As previously reported (Montgomery et al., 2008), robust theta oscillations were seen during REM sleep during the memory consolidation period, with a prominent autocorrelation within the theta band and no difference between $Halo^{WT}$ and $Halo^{nestin}$ mice (Figure 3J). Furthermore, LFPs and theta peaks were similar during light on and off periods between $Halo^{WT}$ (Figure 3K) and $Halo^{nestin}$ mice (Figure 3L). These results indicate that silencing young ABN activity during REM sleep does not influence DG theta oscillations.

Young ABN Activity in REM Sleep Regulates DG Gene Expression

ABN activity finely tunes DG neuron activity (Luna et al., 2019; Toni et al., 2008), which induces new gene expression in REM sleep (Ribeiro et al., 1999). Therefore, we examined the effect of silencing young ABN activity during REM sleep on DG gene

(I) Ca^{2+} imaging of REM+ and REM− ABNs. A, context A; HC, home cage.
(J) Percentage of active (i.e., active more than once) ABNs in each recording period (*$p < 0.05$, **$p < 0.01$, bootstrap; error bars, 95% CI; n = 59 and 36 neurons in REM− and REM+ groups, respectively, from 7 mice).
(K) Percentage of active neurons in each time period (*$p < 0.05$, bootstrap; error bars, 95% CI; n = 60, 36, 72, and 24 neurons in post-shock A−, post-shock A+, test A−, and test A+ groups, respectively, from 7 mice).
gl, granular cell layer; ml, molecular layer; sgz, subgranular zone.

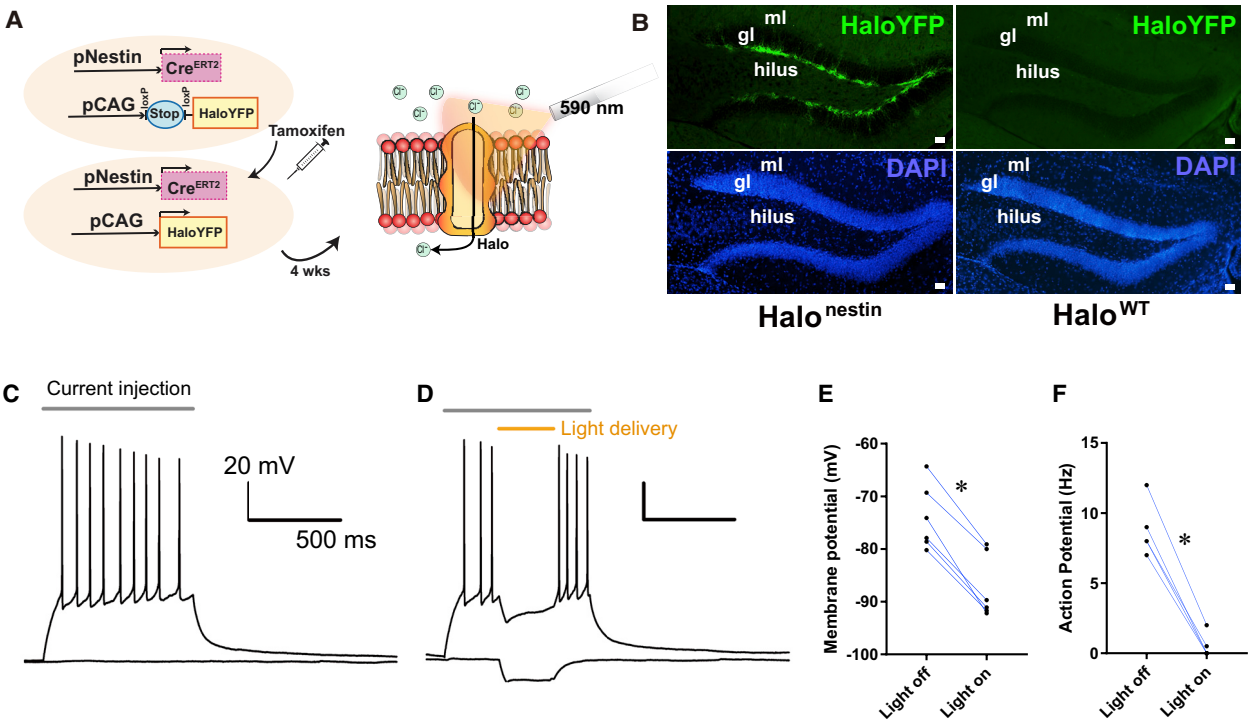

Figure 2. Temporally Specific and Reversible Silencing of Young ABNs by Optogenetic Silencing

(A) Transgenic method.

(B) HaloYFP expression in young ABNs (scale bars, 40 μm).

(C) Current injection (40 pA, gray bar) elicited robust action potential firing (top trace), whereas no action potentials were observed in the absence of the current injection (bottom trace).

(D) Orange light delivery induced hyperpolarization and blocked action potential generation.

(E) Hyperpolarizing effect of orange light (n = 6 neurons; *p < 0.0001, two-tailed paired t test).

(F) Depolarization-induced action potential frequency (n = 5 neurons; *p < 0.0001, two-tailed paired t test).

expression. Immediately after silencing young ABNs in REM sleep during the memory consolidation period (i.e., 6 h after DS conditioning), we performed RNA sequencing of DG tissue (upper blade of the dorsal DG) using laser microdissection microscopy (Figures 4A–4G). Of the 49,585 genes quantified, we found decreased *Zif268* (or *Egr1*), *Gadd45g*, *Npas4*, *Egr2*, *Nr4a1*, *5430416O09Rik*, *Fos*, and *Jhy* expression, and increased *Nestin* expression in Halo^{nestin} mice compared with Halo^{WT} mice (Figures 4H–4J). *Zif268*, *Npas4*, *Egr2*, *Nr4a1*, and *Fos* belong to the immediate early gene family, whose expression in the DG reflects neuronal activity and/or synaptic plasticity (Chen et al., 2014; Cole et al., 1989; Lin et al., 2008; Renouard et al., 2015; Ribeiro et al., 1999, 2002). All genes with decreased expression had motif sequences for the Serum Response Factor (SRF) transcription factor in their promoter/enhancer regions (Figure 4K) despite no change in the expression of SRF itself (Figure 4L). These results suggest that the young ABN activity in REM sleep is required for the expression of activity/synaptic plasticity-related genes, possibly through SRF activity.

Silencing Young ABN Activity in REM Sleep Leads to Elongation of Dendritic Spines

REM sleep prunes and strengthens newly formed spines in the motor cortex after learning (Li et al., 2017), and fear learning induces plasticity-dependent remodeling of ABN dendritic spines (Petsophonsakul et al., 2017). Moreover, SRF activity controls synaptic plasticity (Etkin et al., 2006; Ramanan et al., 2005). Therefore, we hypothesized that young ABN activity during REM sleep induces ABN spine structural remodeling.

To test this hypothesis, we compared ABN spines in REM-silenced and control mice after DS or IS conditioning (Figure 5A). For control mice that underwent DS conditioning, we used no light delivery in Halo^{nestin} mice and orange light delivery in ChR^{nestin} mice, in which young ABNs express channelrhodopsin-2 (H134R)/YFP that is not activated by orange light (Han et al., 2009). As expected, 3D reconstruction of the dendrites of young ABNs (Figure 5B) revealed the presence of dendritic varicosities (Zhao et al., 2010). Compared with IS conditioning, DS conditioning generally increased spine density and head size (Figures 5C and 5D), suggesting that the association of context and shock initiates active remodeling of spines on young ABNs. However, in mice in which young ABN activity was silenced during REM sleep, there was an increase in the length of spine necks (Figure 5E), similar to that observed in ABNs of *Schnurri-2* knockout mice (Nakao et al., 2017), which show a severe working memory deficit (Takao et al., 2013). By contrast, there were no changes in spine density, head diameter, or neck length on fully mature DG granule neurons silenced during

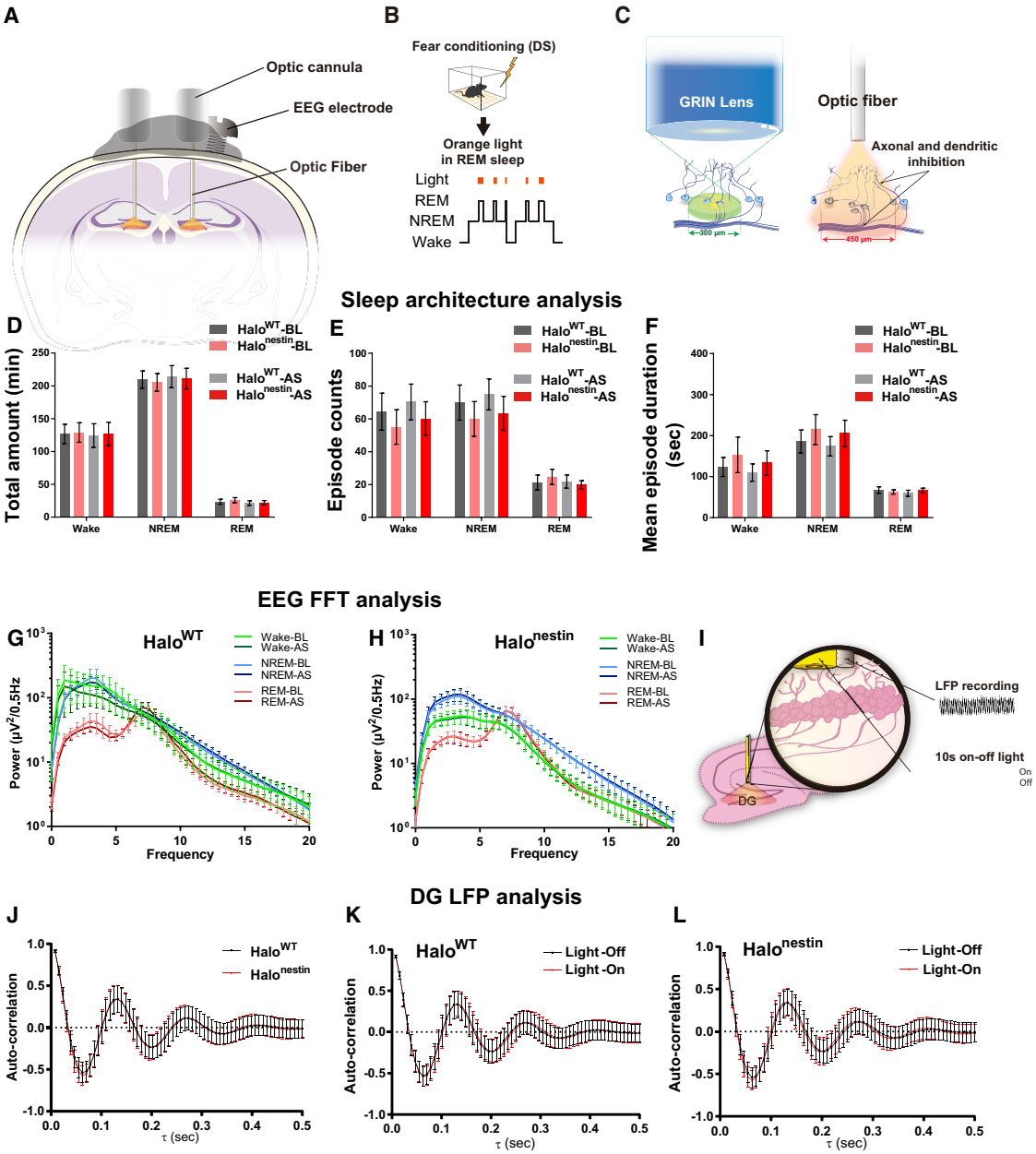

Figure 3. Silencing Young ABN Activity in REM Sleep Does Not Affect Sleep or DG Theta Oscillations

(A and B) EEG electrode and optic cannula implantation (A) for real-time sleep analysis and optogenetic intervention (B).

(C) Difference in effective area between imaging and optogenetic manipulation experiments.

(D–F) Total amount of time (D), episode count (E), and mean episode duration (F) under optogenetic silencing during REM sleep within 6 h after DS (AS: zeitgeber time [ZT] = ~2–8) and a BL recording period (ZT = ~2–8; n = 11–13 mice/genotype; error bars, 95% CI).

(G and H) Fast Fourier transform (FFT) analysis of EEG activity in Halo^{WT} (G) and Halo^{nestin} (H) mice under optogenetic silencing during REM sleep (n = 12–13 mice/group; error bars, 95% CI).

(I) DG LFP recording.

(J) Mean autocorrelation of DG LFPs in REM sleep during memory consolidation (ZT = ~2–8) with their peaks in the theta band for Halo^{WT} (n = 434 epochs) and Halo^{nestin} (n = 468 epochs) mice (τ = 0.11–0.17 s, corresponding to 6–9 Hz; error bars, SD; W = 100.150, p = 0.72, Mann-Whitney test).

(K and L) Mean autocorrelation of DG LFPs during light on and off phases in REM sleep for Halo^{WT} (K; off, n = 205; on, n = 229 epochs; W = 24.240, p = 0.56, Mann-Whitney test) and Halo^{nestin} (L; off, n = 225; on, n = 243 epochs; W = 26.873, p = 0.75, Mann-Whitney test) mice (error bars, SD).

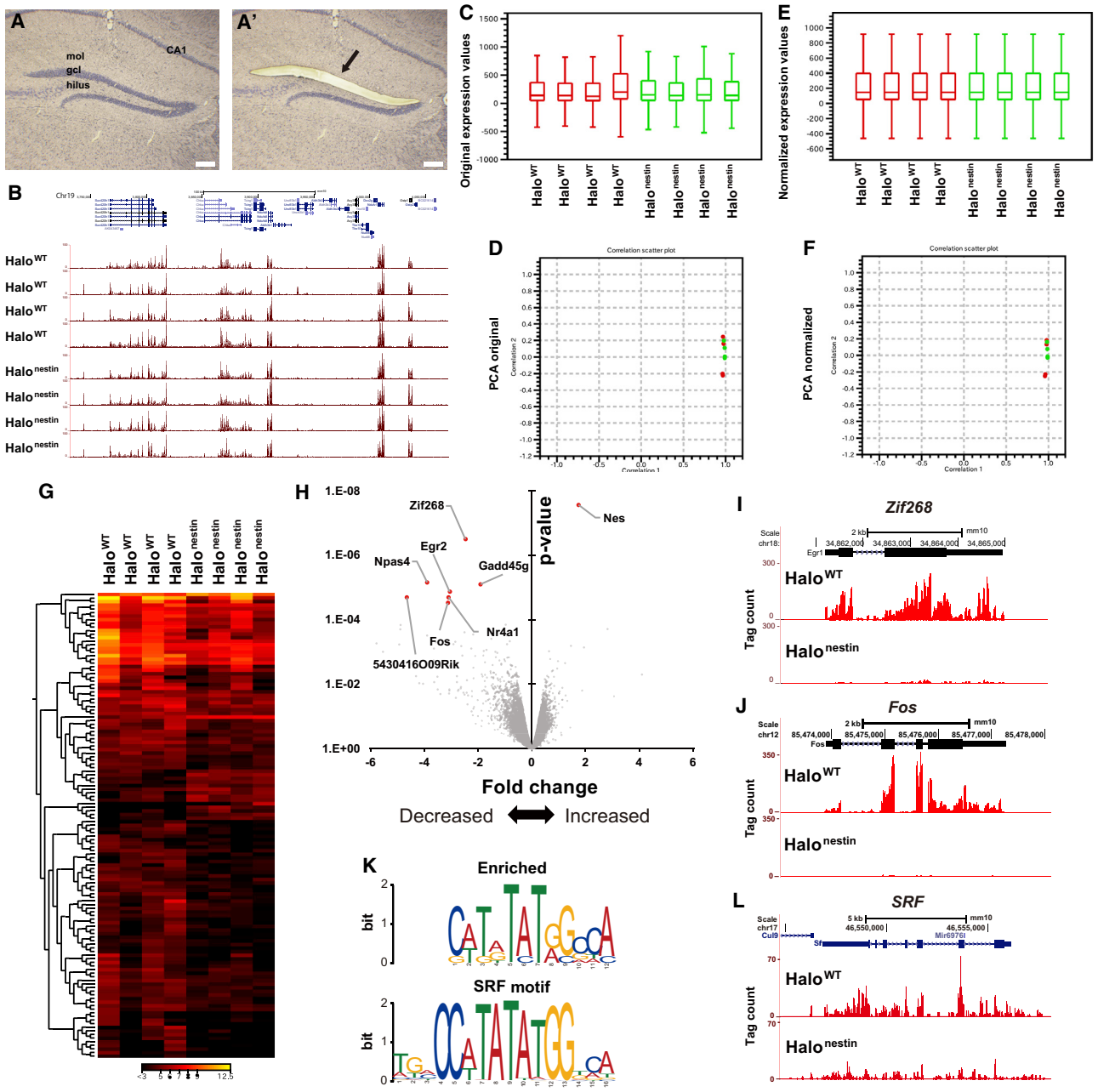

Figure 4. Changes in DG Gene Expression after Silencing of Young ABNs in REM Sleep

(A) Before (A) and after (A') laser micro-dissection of the upper blade of the dorsal DG (scale bar, 100 μm).

(B) Representative UCSC Genome Browser displays of tag counts (red) from each sample in chromosome 19 confirmed consistent data quality (blue, reference transcripts).

(C–F) Boxplot (C and E) and principal-component analysis (PCA) (D and F; red bars, Halo^{WT} mice; green bars, Halo^{nestin} mice) of raw (C and D) and normalized expression values (E and F).

(G) Cluster heatmap showing overview of differentially expressed genes (filtered by raw $p < 0.05$, |fold change| > 2, interquartile range > 10).

(H) Average fold change and p value for Halo^{nestin} versus Halo^{WT} mice (n = 4 mice each).

(I, J, and L) Representative RefSeq sequences (top) and tag counts (red).

(K) The promoter/enhancer regions of all eight genes with decreased expression (top) contained SRF binding sequences (bottom; $p < 0.0001$) despite no change in the expression of SRF itself (L).

See also Data S2.

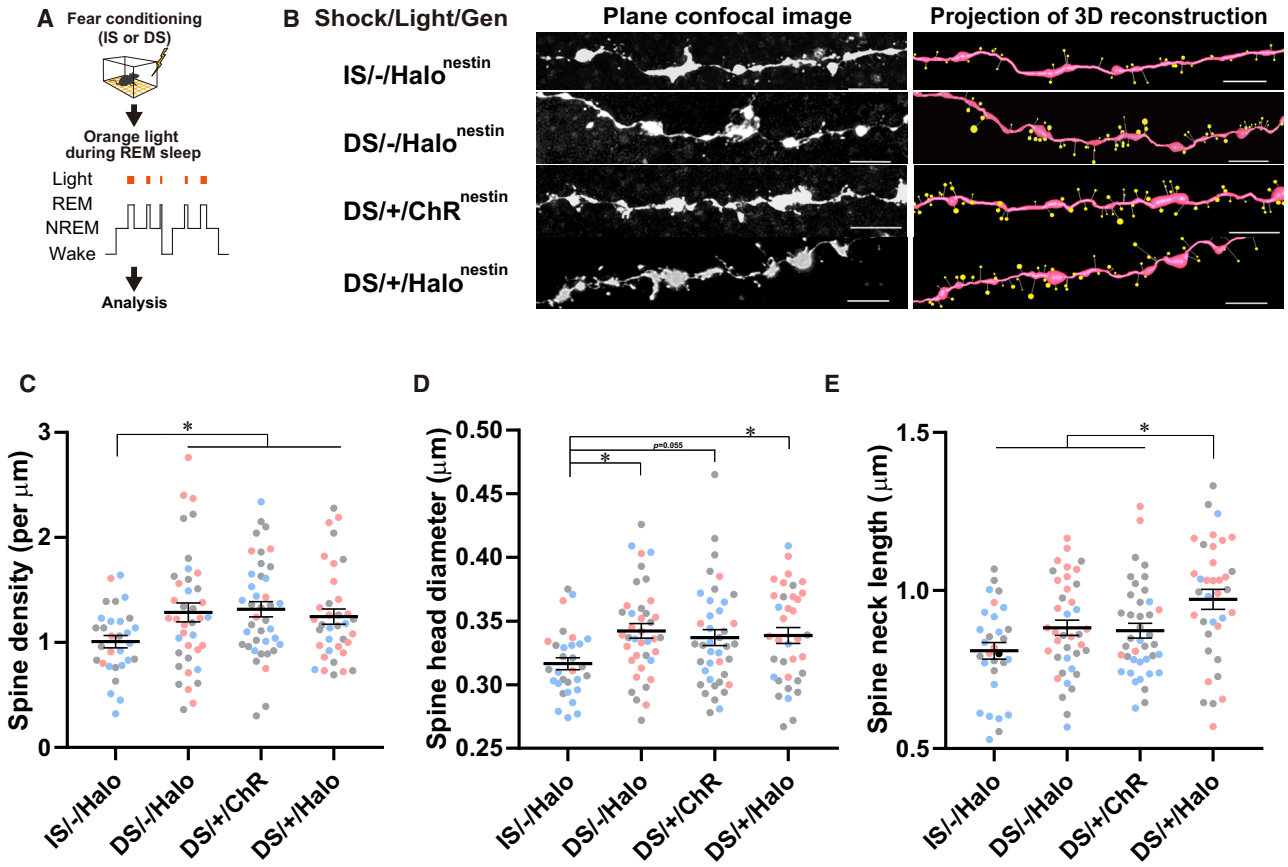

Figure 5. Silencing Young ABN Activity in REM Sleep Leads to Elongation of ABN Dendritic Spines

(A) Experimental paradigm.

(B) 3D reconstruction of confocal images (scale bars, 5 μm).

(C–E) Spine density (C), head diameter (D), and neck length (E). n = 30–40 dendrites/group, error bars, SERM, *p < 0.05, one-way ANOVA with bootstrap methods (C) or Sidak's multiple comparison tests (D and E). Mice within each group are represented by different color markers (red, blue, or gray).

REM sleep (Figures S5D–S5M). Previous studies show that an increase in spine neck length reflects a weakening of overall synaptic strength (Araya et al., 2014) and desynchronization of neural activity from synaptic input (Tanaka et al., 2008). Therefore, these results suggest that the activity of young ABNs in REM sleep increases the robustness of their synapses.

Silencing Young ABN Activity in REM Sleep Impairs Contextual Fear Memory Consolidations

Finally, we examined the role of young ABN activity during REM sleep in memory consolidation. Halo^{nestin} and Halo^{WT} mice that did not undergo optogenetic silencing showed similar levels of freezing during the memory retrieval test (Figures 6A and 6B). However, silencing young ABN activity during REM sleep within the memory consolidation window (total ~11 min light delivery) impaired memory (Figures 6C and 6D), whereas silencing outside the memory consolidation window (i.e., >6 h after DS) had no such effect (Figures 6E and 6F). Reactivity to shock was similar between Halo^{nestin} and Halo^{WT} mice, suggesting that the reduced freezing was not due to motor or sensory deficits (Figures 6G and 6H). These results suggest that the memory deficit induced by silencing young ABN activity during REM sleep is due to impaired memory consolidation.

A longer duration of silencing during NREM sleep (~105 min light delivery) or wakefulness (~21 min light delivery) did not impair memory consolidation (Figures 6I and 6J). Furthermore, no memory impairment was observed when immature (~2-week-old) ABNs were silenced in REM sleep (Figures 6K–6M). The silencing of fully mature (~10-week-old) ABNs tended to reduce freezing (Figures 6K, 6N, and 6O), perhaps because of the inclusion of some young ABNs in the silenced population (Figure S1) (Lagace et al., 2007), but this effect did not reach statistical significance, even with a larger number of mice (n > 17 mice/group, p = 0.084; Figures 6P and 6Q). Moreover, silencing fully mature DG granule neurons during REM sleep did not impair memory (Figures S5N and S5O). These results suggest that young ABNs play a more pronounced role in memory consolidation during REM sleep than their immature or fully mature counterparts. The silencing of young ABN activity in REM sleep did not impair auditory fear memory (Figures 6R and 6S). Because previous work demonstrates that either activation or silencing of ABNs during learning and retrieval impairs fear memory

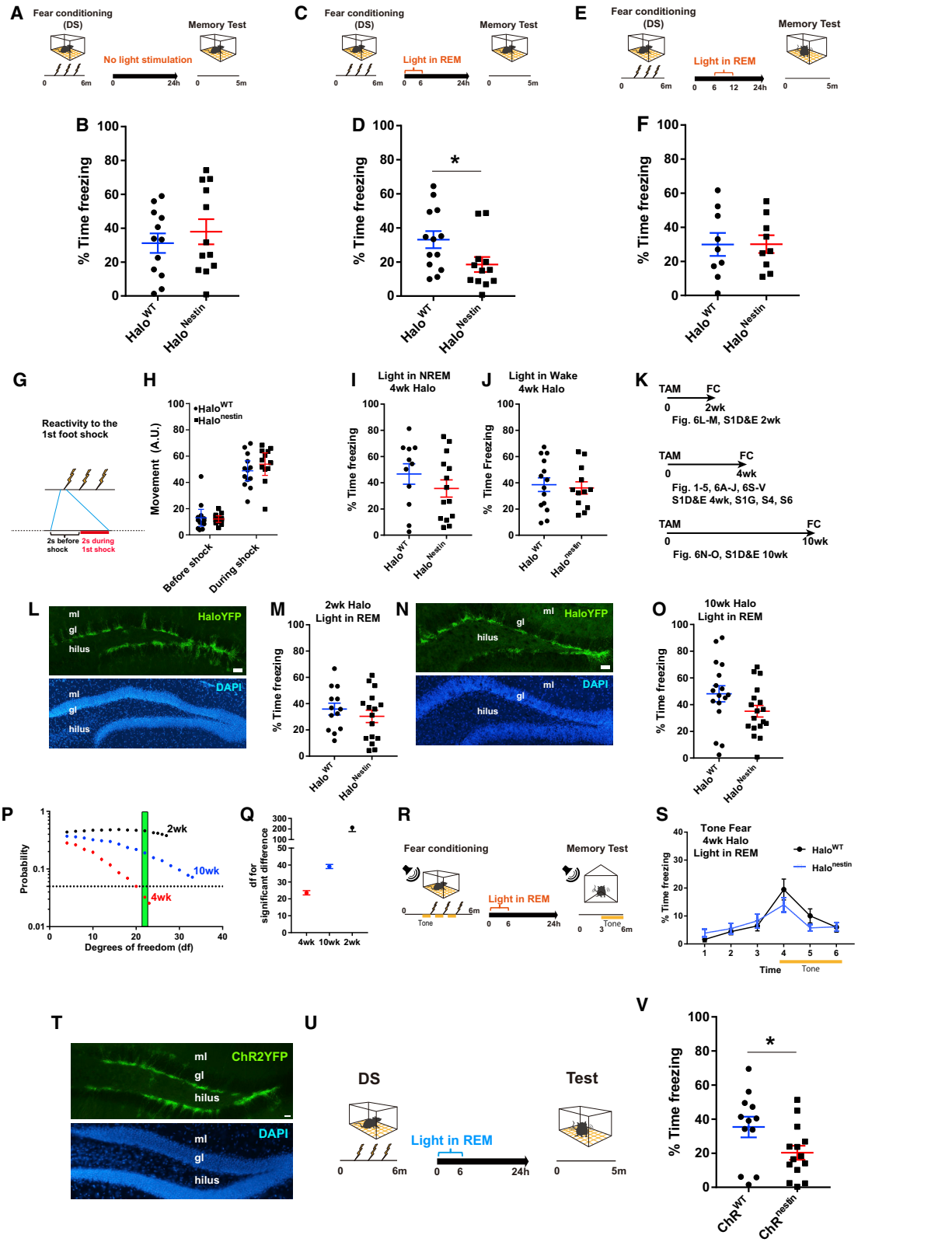

(legend on next page)

(Danielson et al., 2016), we used equivalent transgenic (ChR^{nestin}) mice to determine whether randomly activating young ABNs in REM sleep during the memory consolidation window affects memory. ChR^{nestin} and Cre-negative littermate controls (ChR^{WT}) underwent DS conditioning followed by optogenetic activation during REM sleep (Figures 6T and 6U). The next day, ChR^{nestin} mice showed less freezing than ChR^{WT} mice (Figure 6V), suggesting that randomly increasing young ABN activity during REM sleep interferes with memory consolidation. Together, these results indicate that finely tuned activity of young ABNs in REM sleep is required for the consolidation of contextual fear memory.

DISCUSSION

These findings provide causal evidence that the sparse activity of young ABNs in REM sleep is necessary for memory consolidation. Until now, the activity and function of ABNs in memory consolidation during sleep has been unknown. In addition, the type of hippocampal neuron responsible for memory consolidation during REM sleep was not clear. We found that the acquisition of contextual fear memory reduced the overall activity of young ABNs during REM sleep, but this remnant activity appeared to reflect the reactivation of ABNs that participated in learning. This sparse ABN activity was necessary for memory consolidation, because its silencing altered ABN dendritic spine structures, and both silencing and random activation impaired memory consolidation. These findings identify DG ABNs as a key neuronal population for contextual fear memory consolidation during REM sleep and provide a framework allowing this mechanism to be further explored.

Our results suggest that finely coordinated ABN activity during REM sleep is necessary for memory consolidation based on the observations that: (1) ABN activity decreased during REM sleep only after the formation of an association between a context and shock, (2) ABNs that were active during learning were more likely to be reactivated in subsequent REM sleep during memory consolidation, and (3) disrupting ensemble ABN activity in REM sleep during memory consolidation resulted in an elongation of ABN spine necks and memory deficits. Thus, a sparse and specific population of ABNs that are predominantly active during learning may subsequently undergo synaptic modifications during REM sleep and thereby enable memory consolidation. We speculate that these synaptic modifications depend on the fine-tuning of ABN activity in concert with local REM theta oscillation, because not only silencing but also random activation during REM sleep impaired memory consolidation. Indeed, the theta phase-specific activity of hippocampal neurons determines their contribution to learning or memory retrieval (Hasselmo et al., 2002; Siegle and Wilson, 2014) and modulates synaptic weights via spike-timing-dependent synaptic plasticity in the CA1 (Huerta and Lisman, 1993; Kwag and Paulsen, 2009) and DG (Orr et al., 2001). Therefore, during REM sleep after learning, young ABNs may coordinate their activity with theta rhythm and thereby facilitate a synchrony-based plasticity mechanism for memory consolidation.

Do young ABNs that are active in REM sleep constitute the memory trace? In our experimental setting, young ABNs that were active during the post-shock period, but not those that were active during the memory retrieval test, were more likely to be reactivated during REM sleep. The likelihood of ABN activity during both the post-shock and test periods was not associated with their likelihood of being active during REM sleep. Taken together, these results suggest the following possibilities: (1) young ABN activity during REM sleep is necessary for the consolidation of a memory trace in downstream circuits, and/or (2) the ensemble activity patterns of ABNs that are active in REM sleep constitute a memory trace regardless of the overall population size or activity level of ABNs.

Regarding the first possibility, young ABNs that are active in REM sleep after learning may coordinate the maturation of a memory trace encoded in downstream circuits. Indeed, previous studies demonstrate the highly coordinated and dynamic nature of ABN output to downstream targets (Bergami et al., 2015; Gu et al., 2012; Luna et al., 2019; Marín-Burgin et al., 2012). Therefore, REM sleep may provide a suitable environment for ABNs to form a memory trace in downstream circuitry, perhaps through theta-related mechanisms. Thus, it would be particularly interesting to understand how young ABNs that are active in REM sleep are specifically selected.

Figure 6. Effect of Manipulating Young ABN Activity on Memory Consolidation

(A, C, and E) Behavioral paradigm for no-light stimulation control (A), light during consolidation period (C), and outside the period (E).

(B, D, and F) Freezing without light delivery (B; two-tailed paired t test; n = 12/genotype; error bars, SEM), after optogenetic silencing during REM sleep within (D; n = 12–13/genotype; *p < 0.05, two-tailed unpaired t test; error bars, SEM) or outside the protein synthesis-dependent memory consolidation window (F; n = 9/genotype; p = 0.98, two-tailed unpaired t test; error bars, SEM).

(G and H) Protocol (G) and data (H) for shock reactivity during conditioning (two-way repeated-measures ANOVA, n = 12–13/genotype; error bars, 95% CI).

(I and J) Freezing after silencing young ABN activity in NREM sleep (I) or wakefulness (J) within the memory consolidation window (n = 11–14 mice/genotype; error bars, SEM).

(K) Experimental timelines for labeling the same adult neural progenitors with the same tamoxifen injection protocol.

(L–O) HaloYFP expression (L and N) and freezing (M and O) 2 (L and M; n = 13–16 mice/genotype) or 10 (N and O; n = 17–18 mice/genotype) weeks after tamoxifen injection (error bars, SEM). Scale bars, 40 μm.

(P) Power analysis for each age group. Dotted line indicates threshold of statistical significance (p = 0.05). Green box denotes the minimum degrees of freedom for the 4-week group to cross the threshold.

(Q) Estimated degrees of freedom (df) required to reach statistical significance within each group. Error bars, 95% CI.

(R and S) Freezing (S) after silencing young ABN activity in REM sleep after tone fear conditioning (R) (n = 9 mice/genotype; error bars, SEM).

(T) ChR2YFP expression in young ABNs. Scale bars, 40 μm.

(U) Contextual fear conditioning paradigm.

(V) Freezing after 20-Hz light delivery in REM sleep (*p < 0.05, two-tailed paired t test; n = 10–12/genotype; error bars, SEM).

Regarding the second possibility, a dynamic change in the ensemble activity of young ABNs that are active in REM sleep after learning may constitute the memory trace, similar to that for fear memory formation in the amygdala (Grewe et al., 2017). Although we did not detect differences in average Ca^{2+} event frequency during the memory retrieval test between REM+ and REM− ABNs, this does not rule out the possibility that changes in the activity of each REM+ ABN collectively constitute a population ensemble that represents a memory trace. However, the sparseness of REM+ ABN activity hampered population analysis in this study.

To test these possibilities in the future, ABN activity must be analyzed with higher temporal resolution and more specifically manipulated. Although Ca^{2+} imaging provides a good indication of differences in neural activity between brain states (e.g., wakefulness versus sleep), genetically encoded Ca^{2+} sensors cannot achieve the resolution necessary to assess theta modulation (e.g., Akerboom et al., 2012). Moreover, to specifically select and control ABNs that are active during REM sleep, a method capable of manipulating ABN activity with higher temporal resolution compatible with the short nature of single REM episodes (~1 min) is required. Newly developed technologies may overcome these issues (Adam et al., 2019; Lee et al., 2017; Wang et al., 2017). Nevertheless, our findings indicate that sparse and finely tuned hippocampal ABN activity is necessary for REM sleep-dependent memory consolidation.

STAR★METHODS

Detailed methods are provided in the online version of this paper and include the following:

SUPPLEMENTAL INFORMATION

Supplemental Information can be found online at https://doi.org/10.1016/j.neuron.2020.05.008.

ACKNOWLEDGMENTS

We thank G. Kempermann and K.G. Akers for comments on the manuscript. We thank all WPI-IIIS members; T. Tezuka, S. Yaghisita, K. Kobayakawa, R. Kobayakawa, K. Shikama, S. Sugimori, N. Hasegawa, T. Hosokawa, A. Oba, and Y. Mimura for technical assistance; and J. Naughton (GT3 Core Facility of the Salk Institute) for retroviral preparation. This work was partially supported by grants from the World Premier International Research Center Initiative from MEXT, JST CREST (grant JPMJCR1655), JSPS KAKENHI (grants 16K18359, 15F15408, 26115502, 25116530, JP16H06280, 19F19310, and 20H03552), Takeda Science Foundation, Shimadzu Science Foundation, Kanae Foundation, Research Foundation for Opto-Science and Technology, Ichiro Kanehara Foundation, Kato Memorial Bioscience Foundation, Japan Foundation for Applied Enzymology, SENSHIN Medical Research Foundation, Life Science Foundation of Japan, Uehara Memorial Foundation, Brain Science Foundation, Kowa Life Science Foundation, Inamori Research Grants Program, and GSK Japan (to M.S.); JSPS KAKENHI (grants 25000015 and 18H04012 to M. Kano); Tokyo Biochemical Research Foundation and JSPS FPD (to S. Srinivasan); and JSPS FPD (to D.K.).

AUTHOR CONTRIBUTIONS

Conceptualization, M.S. and D.K.; Methodology, D.K., I.K., A.C.-R., P.V., S. Srinivasan, Y.S., M. Kasuya, T.-S.Y., K.V., M.M., T.O., C.T., S.W., P.N., N.K., T.J.M., and M.S.; Investigation, D.K., I.K., A.C.-R., S. Srinivasan, Y.S., M. Kasuya, T.-S.Y., K.V., M.M., S. Singh, C.T., Y.C., T.N., P.N., N.K., and M.S.; Validation, D.K., I.K., S. Srinivasan, S. Singh, T.N., and M.S.; Formal Analysis, P.V., M.M., T.O., I.K., and M.S.; Data Curation, I.K. and M.S.; Visualization, D.K., P.V., M.M., T.O., I.K., and M.S.; Writing – Original Draft, M.S.; Writing – Review & Editing, M.S., T.J.M., S.-H.W., K.S., M. Kasuya, P.V., T.O., M.M., T.-S.Y., M.Y., D.K., M. Kano, K.V., Y.S., and T.S.; Funding Acquisition, M.S., M.Y., T.S., S.G.K., Y.S., D.K., S. Srinivasan, and M. Kano; Resources, M.S., T.S., S.G.K., S.K., M. Kano, and M.Y.; Supervision, M.S., D.K., T.S., M.Y., S.G.K., S.K., and M. Kano; Project Administration, D.K., I.K., and M.S. All authors discussed and approved the manuscript.

DECLARATION OF INTERESTS

The authors declare no competing interests.

Received: June 17, 2019
Revised: March 21, 2020
Accepted: May 6, 2020
Published: June 4, 2020

REFERENCES

Adam, Y., Kim, J.J., Lou, S., Zhao, Y., Xie, M.E., Brinks, D., Wu, H., Mostajo-Radji, M.A., Kheifets, S., Parot, V., et al. (2019). Voltage imaging and optogenetics reveal behaviour-dependent changes in hippocampal dynamics. Nature *569*, 413–417.

Akerboom, J., Chen, T.W., Wardill, T.J., Tian, L., Marvin, J.S., Mutlu, S., Calderón, N.C., Esposti, F., Borghuis, B.G., Sun, X.R., et al. (2012). Optimization of a GCaMP calcium indicator for neural activity imaging. J. Neurosci. *32*, 13819–13840.

Akers, K.G., Martinez-Canabal, A., Restivo, L., Yiu, A.P., De Cristofaro, A., Hsiang, H.L., Wheeler, A.L., Guskjolen, A., Niibori, Y., Shoji, H., et al. (2014). Hippocampal neurogenesis regulates forgetting during adulthood and infancy. Science *344*, 598–602.

Alam, M.J., Kitamura, T., Saitoh, Y., Ohkawa, N., Kondo, T., and Inokuchi, K. (2018). Adult neurogenesis conserves hippocampal memory capacity. J. Neurosci. *38*, 6854–6863.

Allen, T.A., and Fortin, N.J. (2013). The evolution of episodic memory. Proc. Natl. Acad. Sci. USA *110* (*Suppl 2*), 10379–10386.

Altman, J., and Das, G.D. (1965). Autoradiographic and histological evidence of postnatal hippocampal neurogenesis in rats. J. Comp. Neurol. *124*, 319–335.

Araya, R., Vogels, T.P., and Yuste, R. (2014). Activity-dependent dendritic spine neck changes are correlated with synaptic strength. Proc. Natl. Acad. Sci. USA *111*, E2895–E2904.

Bergami, M., Masserdotti, G., Temprana, S.G., Motori, E., Eriksson, T.M., Göbel, J., Yang, S.M., Conzelmann, K.K., Schinder, A.F., Götz, M., and Berninger, B. (2015). A critical period for experience-dependent remodeling of adult-born neuron connectivity. Neuron *85*, 710–717.

Blanchard, R.J., Fukunaga, K.K., and Blanchard, D.C. (1976). Environmental control of defensive reactions to footshock. Bull. Psychon. Soc. *8*, 129–130.

Boldrini, M., Fulmore, C.A., Tartt, A.N., Simeon, L.R., Pavlova, I., Poposka, V., Rosoklija, G.B., Stankov, A., Arango, V., Dwork, A.J., et al. (2018). Human Hippocampal Neurogenesis Persists throughout Aging. Cell Stem Cell *22*, 589–599.e5.

Bourtchouladze, R., Abel, T., Berman, N., Gordon, R., Lapidus, K., and Kandel, E.R. (1998). Different training procedures recruit either one or two critical periods for contextual memory consolidation, each of which requires protein synthesis and PKA. Learn. Mem. *5*, 365–374.

Boyce, R., Glasgow, S.D., Williams, S., and Adamantidis, A. (2016). Causal evidence for the role of REM sleep theta rhythm in contextual memory consolidation. Science *352*, 812–816.

Chen, Y., Wang, Y., Ertürk, A., Kallop, D., Jiang, Z., Weimer, R.M., Kaminker, J., and Sheng, M. (2014). Activity-induced Nr4a1 regulates spine density and distribution pattern of excitatory synapses in pyramidal neurons. Neuron *83*, 431–443.

Clelland, C.D., Choi, M., Romberg, C., Clemenson, G.D., Jr., Fragniere, A., Tyers, P., Jessberger, S., Saksida, L.M., Barker, R.A., Gage, F.H., and Bussey, T.J. (2009). A functional role for adult hippocampal neurogenesis in spatial pattern separation. Science *325*, 210–213.

Cole, A.J., Saffen, D.W., Baraban, J.M., and Worley, P.F. (1989). Rapid increase of an immediate early gene messenger RNA in hippocampal neurons by synaptic NMDA receptor activation. Nature *340*, 474–476.

Danielson, N.B., Kaifosh, P., Zaremba, J.D., Lovett-Barron, M., Tsai, J., Denny, C.A., Balough, E.M., Goldberg, A.R., Drew, L.J., Hen, R., et al. (2016). Distinct contribution of adult-born hippocampal granule cells to context encoding. Neuron *90*, 101–112.

Dere, E., Huston, J.P., and De Souza Silva, M.A. (2005). Integrated memory for objects, places, and temporal order: evidence for episodic-like memory in mice. Neurobiol. Learn. Mem. *84*, 214–221.

Dolorfo, C.L., and Amaral, D.G. (1998). Entorhinal cortex of the rat: topographic organization of the cells of origin of the perforant path projection to the dentate gyrus. J. Comp. Neurol. *398*, 25–48.

Duan, H., Wearne, S.L., Morrison, J.H., and Hof, P.R. (2002). Quantitative analysis of the dendritic morphology of corticocortical projection neurons in the macaque monkey association cortex. Neuroscience *114*, 349–359.

Eriksson, P.S., Perfilieva, E., Björk-Eriksson, T., Alborn, A.M., Nordborg, C., Peterson, D.A., and Gage, F.H. (1998). Neurogenesis in the adult human hippocampus. Nat. Med. *4*, 1313–1317.

Etkin, A., Alarcón, J.M., Weisberg, S.P., Touzani, K., Huang, Y.Y., Nordheim, A., and Kandel, E.R. (2006). A role in learning for SRF: deletion in the adult forebrain disrupts LTD and the formation of an immediate memory of a novel context. Neuron *50*, 127–143.

Fanselow, M.S. (1986). Associative vs topographical accounts of the immediate shock-freezing deficit in rats: Implications for the response selection rules governing species-specific defensive reactions. Learn. Motiv. *17*, 16–39.

Forni, P.E., Scuoppo, C., Imayoshi, I., Taulli, R., Dastrù, W., Sala, V., Betz, U.A., Muzzi, P., Martinuzzi, D., Vercelli, A.E., et al. (2006). High levels of Cre expression in neuronal progenitors cause defects in brain development leading to microencephaly and hydrocephaly. J. Neurosci. *26*, 9593–9602.

Gao, Z., Ure, K., Ables, J.L., Lagace, D.C., Nave, K.A., Goebbels, S., Eisch, A.J., and Hsieh, J. (2009). Neurod1 is essential for the survival and maturation of adult-born neurons. Nat. Neurosci. *12*, 1090–1092.

Ge, S., Yang, C.H., Hsu, K.S., Ming, G.L., and Song, H. (2007). A critical period for enhanced synaptic plasticity in newly generated neurons of the adult brain. Neuron *54*, 559–566.

Ghandour, K., Ohkawa, N., Fung, C.C.A., Asai, H., Saitoh, Y., Takekawa, T., Okubo-Suzuki, R., Soya, S., Nishizono, H., Matsuo, M., et al. (2019). Orchestrated ensemble activities constitute a hippocampal memory engram. Nat. Commun. *10*, 2637.

Ghosh, K.K., Burns, L.D., Cocker, E.D., Nimmerjahn, A., Ziv, Y., Gamal, A.E., and Schnitzer, M.J. (2011). Miniaturized integration of a fluorescence microscope. Nat. Methods *8*, 871–878.

Girardeau, G., Benchenane, K., Wiener, S.I., Buzsáki, G., and Zugaro, M.B. (2009). Selective suppression of hippocampal ripples impairs spatial memory. Nat. Neurosci. *12*, 1222–1223.

Gonzalez, W.G., Zhang, H., Harutyunyan, A., and Lois, C. (2019). Persistence of neuronal representations through time and damage in the hippocampus. Science *365*, 821–825.

Grewe, B.F., Gründemann, J., Kitch, L.J., Lecoq, J.A., Parker, J.G., Marshall, J.D., Larkin, M.C., Jercog, P.E., Grenier, F., Li, J.Z., et al. (2017). Neural ensemble dynamics underlying a long-term associative memory. Nature *543*, 670–675.

Gu, Y., Arruda-Carvalho, M., Wang, J., Janoschka, S.R., Josselyn, S.A., Frankland, P.W., and Ge, S. (2012). Optical controlling reveals time-dependent roles for adult-born dentate granule cells. Nat. Neurosci. *15*, 1700–1706.

Guo, W., Allan, A.M., Zong, R., Zhang, L., Johnson, E.B., Schaller, E.G., Murthy, A.C., Goggin, S.L., Eisch, A.J., Oostra, B.A., et al. (2011). Ablation of Fmrp in adult neural stem cells disrupts hippocampus-dependent learning. Nat. Med. *17*, 559–565.

Han, X., Qian, X., Stern, P., Chuong, A.S., and Boyden, E.S. (2009). Informational lesions: optical perturbation of spike timing and neural synchrony via microbial opsin gene fusions. Front. Mol. Neurosci. *2*, 12.

Hasselmo, M.E., Bodelón, C., and Wyble, B.P. (2002). A proposed function for hippocampal theta rhythm: separate phases of encoding and retrieval enhance reversal of prior learning. Neural Comput. *14*, 793–817.

Hojo, Y., Munetomo, A., Mukai, H., Ikeda, M., Sato, R., Hatanaka, Y., Murakami, G., Komatsuzaki, Y., Kimoto, T., and Kawato, S. (2015). Estradiol rapidly modulates spinogenesis in hippocampal dentate gyrus: Involvement of kinase networks. Horm. Behav. *74*, 149–156.

Huckleberry, K.A., Shue, F., Copeland, T., Chitwood, R.A., Yin, W., and Drew, M.R. (2018). Dorsal and ventral hippocampal adult-born neurons contribute to context fear memory. Neuropsychopharmacology *43*, 2487–2496.

Huerta, P.T., and Lisman, J.E. (1993). Heightened synaptic plasticity of hippocampal CA1 neurons during a cholinergically induced rhythmic state. Nature *364*, 723–725.

Imayoshi, I., Sakamoto, M., Ohtsuka, T., Takao, K., Miyakawa, T., Yamaguchi, M., Mori, K., Ikeda, T., Itohara, S., and Kageyama, R. (2008). Roles of continuous neurogenesis in the structural and functional integrity of the adult forebrain. Nat. Neurosci. *11*, 1153–1161.

Jimenez, J.C., Su, K., Goldberg, A.R., Luna, V.M., Biane, J.S., Ordek, G., Zhou, P., Ong, S.K., Wright, M.A., Zweifel, L., et al. (2018). Anxiety cells in a hippocampal-hypothalamic circuit. Neuron *97*, 670–683.e6.

Kee, N., Teixeira, C.M., Wang, A.H., and Frankland, P.W. (2007). Preferential incorporation of adult-generated granule cells into spatial memory networks in the dentate gyrus. Nat. Neurosci. *10*, 355–362.

Kempermann, G. (2012). New neurons for 'survival of the fittest'. Nat. Rev. Neurosci. *13*, 727–736.

Kishimoto, Y., Cagniard, B., Yamazaki, M., Nakayama, J., Sakimura, K., Kirino, Y., and Kano, M. (2015). Task-specific enhancement of hippocampus-dependent learning in mice deficient in monoacylglycerol lipase, the major hydrolyzing enzyme of the endocannabinoid 2-arachidonoylglycerol. Front. Behav. Neurosci. *9*, 134.

Kitamura, T., Saitoh, Y., Takashima, N., Murayama, A., Niibori, Y., Ageta, H., Sekiguchi, M., Sugiyama, H., and Inokuchi, K. (2009). Adult neurogenesis modulates the hippocampus-dependent period of associative fear memory. Cell *139*, 814–827.

Knobloch, M., Braun, S.M.G., Zurkirchen, L., von Schoultz, C., Zamboni, N., Araúzo-Bravo, M.J., Kovacs, W.J., Karalay, O., Suter, U., Machado, R.A.C., et al. (2013). Metabolic control of adult neural stem cell activity by Fasn-dependent lipogenesis. Nature *493*, 226–230.

Kumar, D., Dedic, N., Flachskamm, C., Voulé, S., Deussing, J.M., and Kimura, M. (2015). Cacna1c (Cav1.2) modulates electroencephalographic rhythm and rapid eye movement sleep recovery. Sleep *38*, 1371–1380.

Kwag, J., and Paulsen, O. (2009). The timing of external input controls the sign of plasticity at local synapses. Nat. Neurosci. *12*, 1219–1221.

Lagace, D.C., Whitman, M.C., Noonan, M.A., Ables, J.L., DeCarolis, N.A., Arguello, A.A., Donovan, M.H., Fischer, S.J., Farnbauch, L.A., Beech, R.D., et al. (2007). Dynamic contribution of nestin-expressing stem cells to adult neurogenesis. J. Neurosci. *27*, 12623–12629.

Lazarus, M., Shen, H.Y., Cherasse, Y., Qu, W.M., Huang, Z.L., Bass, C.E., Winsky-Sommerer, R., Semba, K., Fredholm, B.B., Boison, D., et al. (2011). Arousal effect of caffeine depends on adenosine A2A receptors in the shell of the nucleus accumbens. J. Neurosci. *31*, 10067–10075.

Lee, D., Hyun, J.H., Jung, K., Hannan, P., and Kwon, H.B. (2017). A calcium- and light-gated switch to induce gene expression in activated neurons. Nat. Biotechnol. *35*, 858–863.

Li, W., Ma, L., Yang, G., and Gan, W.B. (2017). REM sleep selectively prunes and maintains new synapses in development and learning. Nat. Neurosci. *20*, 427–437.

Lin, Y., Bloodgood, B.L., Hauser, J.L., Lapan, A.D., Koon, A.C., Kim, T.-K., Hu, L.S., Malik, A.N., and Greenberg, M.E. (2008). Activity-dependent regulation of inhibitory synapse development by Npas4. Nature *455*, 1198–1204.

Louie, K., and Wilson, M.A. (2001). Temporally structured replay of awake hippocampal ensemble activity during rapid eye movement sleep. Neuron *29*, 145–156.

Luna, V.M., Anacker, C., Burghardt, N.S., Khandaker, H., Andreu, V., Millette, A., Leary, P., Ravenelle, R., Jimenez, J.C., Mastrodonato, A., et al. (2019). Adult-born hippocampal neurons bidirectionally modulate entorhinal inputs into the dentate gyrus. Science *364*, 578–583.

Marín-Burgin, A., Mongiat, L.A., Pardi, M.B., and Schinder, A.F. (2012). Unique processing during a period of high excitation/inhibition balance in adult-born neurons. Science *335*, 1238–1242.

Marshall, L., Helgadóttir, H., Mölle, M., and Born, J. (2006). Boosting slow oscillations during sleep potentiates memory. Nature *444*, 610–613.

McHugh, T.J., and Tonegawa, S. (2007). Spatial exploration is required for the formation of contextual fear memory. Behav. Neurosci. *121*, 335–339.

Miyamoto, D., Hirai, D., Fung, C.C.A., Inutsuka, A., Odagawa, M., Suzuki, T., Boehringer, R., Adaikkan, C., Matsubara, C., Matsuki, N., et al. (2016). Top-down cortical input during NREM sleep consolidates perceptual memory. Science *352*, 1315–1318.

Montgomery, S.M., Sirota, A., and Buzsáki, G. (2008). Theta and gamma coordination of hippocampal networks during waking and rapid eye movement sleep. J. Neurosci. *28*, 6731–6741.

Moreno-Jiménez, E.P., Flor-García, M., Terreros-Roncal, J., Rábano, A., Cafini, F., Pallas-Bazarra, N., Ávila, J., and Llorens-Martín, M. (2019). Adult hippocampal neurogenesis is abundant in neurologically healthy subjects and drops sharply in patients with Alzheimer's disease. Nat. Med. *25*, 554–560.

Mukai, H., Hatanaka, Y., Mitsuhashi, K., Hojo, Y., Komatsuzaki, Y., Sato, R., Murakami, G., Kimoto, T., and Kawato, S. (2011). Automated analysis of spines from confocal laser microscopy images: application to the discrimination of androgen and estrogen effects on spinogenesis. Cereb. Cortex *21*, 2704–2711.

Nakao, A., Miyazaki, N., Ohira, K., Hagihara, H., Takagi, T., Usuda, N., Ishii, S., Murata, K., and Miyakawa, T. (2017). Immature morphological properties in subcellular-scale structures in the dentate gyrus of Schnurri-2 knockout mice: a model for schizophrenia and intellectual disability. Mol. Brain *10*, 60.

Nakashiba, T., Cushman, J.D., Pelkey, K.A., Renaudineau, S., Buhl, D.L., McHugh, T.J., Rodriguez Barrera, V., Chittajallu, R., Iwamoto, K.S., McBain, C.J., et al. (2012). Young dentate granule cells mediate pattern separation, whereas old granule cells facilitate pattern completion. Cell *149*, 188–201.

Ninkovic, J., Steiner-Mezzadri, A., Jawerka, M., Akinci, U., Masserdotti, G., Petricca, S., Fischer, J., von Holst, A., Beckers, J., Lie, C.D., et al. (2013). The BAF complex interacts with Pax6 in adult neural progenitors to establish a neurogenic cross-regulatory transcriptional network. Cell Stem Cell *13*, 403–418.

Norimoto, H., Makino, K., Gao, M., Shikano, Y., Okamoto, K., Ishikawa, T., Sasaki, T., Hioki, H., Fujisawa, S., and Ikegaya, Y. (2018). Hippocampal ripples down-regulate synapses. Science *359*, 1524–1527.

Orr, G., Rao, G., Houston, F.P., McNaughton, B.L., and Barnes, C.A. (2001). Hippocampal synaptic plasticity is modulated by theta rhythm in the fascia dentata of adult and aged freely behaving rats. Hippocampus *11*, 647–654.

Park, S., Kramer, E.E., Mercaldo, V., Rashid, A.J., Insel, N., Frankland, P.W., and Josselyn, S.A. (2016). Neuronal allocation to a hippocampal engram. Neuropsychopharmacology *41*, 2987–2993.

Petsophonsakul, P., Richetin, K., Andraini, T., Roybon, L., and Rampon, C. (2017). Memory formation orchestrates the wiring of adult-born hippocampal neurons into brain circuits. Brain Struct. Funct. *222*, 2585–2601.

Pnevmatikakis, E.A., and Giovannucci, A. (2017). NoRMCorre: An online algorithm for piecewise rigid motion correction of calcium imaging data. J. Neurosci. Methods *291*, 83–94.

Purple, R.J., Sakurai, T., and Sakaguchi, M. (2017). Auditory conditioned stimulus presentation during NREM sleep impairs fear memory in mice. Sci. Rep. *7*, 46247.

Quinlan, A.R., and Hall, I.M. (2010). BEDTools: a flexible suite of utilities for comparing genomic features. Bioinformatics *26*, 841–842.

Ramanan, N., Shen, Y., Sarsfield, S., Lemberger, T., Schütz, G., Linden, D.J., and Ginty, D.D. (2005). SRF mediates activity-induced gene expression and synaptic plasticity but not neuronal viability. Nat. Neurosci. *8*, 759–767.

Renouard, L., Billwiller, F., Ogawa, K., Clément, O., Camargo, N., Abdelkarim, M., Gay, N., Scoté-Blachon, C., Touré, R., Libourel, P.-A.P.-A.P., et al. (2015). The supramammillary nucleus and the claustrum activate the cortex during REM sleep. Sci. Adv. *1*, e1400177.

Ribeiro, S., Goyal, V., Mello, C.V., and Pavlides, C. (1999). Brain gene expression during REM sleep depends on prior waking experience. Learn. Mem. *6*, 500–508.

Ribeiro, S., Mello, C.V., Velho, T., Gardner, T.J., Jarvis, E.D., and Pavlides, C. (2002). Induction of hippocampal long-term potentiation during waking leads to increased extrahippocampal zif-268 expression during ensuing rapid-eye-movement sleep. J. Neurosci. *22*, 10914–10923.

Sahay, A., Scobie, K.N., Hill, A.S., O'Carroll, C.M., Kheirbek, M.A., Burghardt, N.S., Fenton, A.A.A., Dranovsky, A., and Hen, R. (2011). Increasing adult hippocampal neurogenesis is sufficient to improve pattern separation. Nature *472*, 466–470.

Sheintuch, L., Rubin, A., Brande-Eilat, N., Geva, N., Sadeh, N., Pinchasof, O., and Ziv, Y. (2017). Tracking the Same Neurons across Multiple Days in Ca^{2+} Imaging Data. Cell Rep. *21*, 1102–1115.

Shors, T.J., Miesegaes, G., Beylin, A., Zhao, M., Rydel, T., and Gould, E. (2001). Neurogenesis in the adult is involved in the formation of trace memories. Nature *410*, 372–376.

Siegle, J.H., and Wilson, M.A. (2014). Enhancement of encoding and retrieval functions through theta phase-specific manipulation of hippocampus. eLife *3*, e03061.

Sorrells, S.F., Paredes, M.F., Cebrian-Silla, A., Sandoval, K., Qi, D., Kelley, K.W., James, D., Mayer, S., Chang, J., Auguste, K.I., et al. (2018). Human hippocampal neurogenesis drops sharply in children to undetectable levels in adults. Nature *555*, 377–381.

Stefanelli, T., Bertollini, C., Lüscher, C., Muller, D., and Mendez, P. (2016). Hippocampal somatostatin interneurons control the size of neuronal memory ensembles. Neuron *89*, 1074–1085.

Takao, K., Kobayashi, K., Hagihara, H., Ohira, K., Shoji, H., Hattori, S., Koshimizu, H., Umemori, J., Toyama, K., Nakamura, H.K., et al. (2013). Deficiency of schnurri-2, an MHC enhancer binding protein, induces mild chronic inflammation in the brain and confers molecular, neuronal, and behavioral phenotypes related to schizophrenia. Neuropsychopharmacology *38*, 1409–1425.

Tanaka, J., Horiike, Y., Matsuzaki, M., Miyazaki, T., Ellis-Davies, G.C.R., and Kasai, H. (2008). Protein synthesis and neurotrophin-dependent structural plasticity of single dendritic spines. Science *319*, 1683–1687.

Tian, L., Hires, S.A., Mao, T., Huber, D., Chiappe, M.E., Chalasani, S.H., Petreanu, L., Akerboom, J., McKinney, S.A., Schreiter, E.R., et al. (2009). Imaging neural activity in worms, flies and mice with improved GCaMP calcium indicators. Nat. Methods *6*, 875–881.

Tiscornia, G., Singer, O., and Verma, I.M. (2006). Production and purification of lentiviral vectors. Nat. Protoc. *1*, 241–245.

Toni, N., Laplagne, D.A., Zhao, C., Lombardi, G., Ribak, C.E., Gage, F.H., and Schinder, A.F. (2008). Neurons born in the adult dentate gyrus form functional synapses with target cells. Nat. Neurosci. *11*, 901–907.

Vargha-Khadem, F., Gadian, D.G., Watkins, K.E., Connelly, A., Van Paesschen, W., and Mishkin, M. (1997). Differential effects of early hippocampal pathology on episodic and semantic memory. Science *277*, 376–380.

Wang, W., Wildes, C.P., Pattarabanjird, T., Sanchez, M.I., Glober, G.F., Matthews, G.A., Tye, K.M., and Ting, A.Y. (2017). A light- and calcium-gated transcription factor for imaging and manipulating activated neurons. Nat. Biotechnol. *35*, 864–871.

Willadt, S., Canepari, M., Yan, P., Loew, L.M., and Vogt, K.E. (2014). Combined optogenetics and voltage sensitive dye imaging at single cell resolution. Front. Cell. Neurosci. *8*, 311.

Wilson, M.A., and McNaughton, B.L. (1994). Reactivation of Hippocampal Ensemble Memories During Sleep. Science *265*, 676–679.

Yang, G., Lai, C.S.W., Cichon, J., Ma, L., Li, W., and Gan, W.-B. (2014). Sleep promotes branch-specific formation of dendritic spines after learning. Science *344*, 1173–1178.

Zambrowicz, B.P., Imamoto, A., Fiering, S., Herzenberg, L.A., Kerr, W.G., and Soriano, P. (1997). Disruption of overlapping transcripts in the ROSA beta geo 26 gene trap strain leads to widespread expression of beta-galactosidase in mouse embryos and hematopoietic cells. Proc. Natl. Acad. Sci. USA *94*, 3789–3794.

Zhang, F., Wang, L.-P., Brauner, M., Liewald, J.F., Kay, K., Watzke, N., Wood, P.G., Bamberg, E., Nagel, G., Gottschalk, A., and Deisseroth, K. (2007). Multimodal fast optical interrogation of neural circuitry. Nature *446*, 633–639.

Zhao, S., Zhou, Y., Gross, J., Miao, P., Qiu, L., Wang, D., Chen, Q., and Feng, G. (2010). Fluorescent labeling of newborn dentate granule cells in GAD67-GFP transgenic mice: a genetic tool for the study of adult neurogenesis. PLoS ONE *5*, e12506.

Zhou, P., Resendez, S.L., Rodriguez-Romaguera, J., Jimenez, J.C., Neufeld, S.Q., Giovannucci, A., Friedrich, J., Pnevmatikakis, E.A., Stuber, G.D., Hen, R., et al. (2018). Efficient and accurate extraction of in vivo calcium signals from microendoscopic video data. eLife *7*, e28728.

Zhuo, J.-M., Tseng, H.A., Desai, M., Bucklin, M.E., Mohammed, A.I., Robinson, N.T., Boyden, E.S., Rangel, L.M., Jasanoff, A.P., Gritton, H.J., and Han, X. (2016). Young adult born neurons enhance hippocampal dependent performance via influences on bilateral networks. eLife *5*, e22429.

STAR★METHODS

KEY RESOURCES TABLE

REAGENT/RESOURCE	SOURCE	IDENTIFIER(S)
Antibodies		
Anti-NeuN mouse IgG antibody	Millipore	MAB377; RRID:AB_2298772
Anti-GFP rabbit IgG antibody	Thermo Fisher	A11122; RRID:AB_221569
Anti-Dcx goat IgG antibody	Santa Cruz Biotechnology	sc-8066; AB_2088494
Alexa Fluor 488 conjugated anti-Mouse IgG antibody F(ab')2 fragment	Jackson Immunoresearch Laboratories	715-546-151; RRID:AB_2340850
biotin conjugated anti-Goat IgG antibody F(ab')2 fragment	Jackson Immunoresearch Laboratories	705-066-147; RRID: AB_2340398
Virus		
pAAV-pEF1a-mCherry-IRES-WGACre	a gift from Dr. Karl Deisseroth, Stanford University	N/A
pENN.AAV.CamKII 0.4.Cre.SV40	a gift from Dr. James M. Wilson (Addgene plasmid # 105558)	#105558; RRID:Addgene_105558
Transgenic Mice		
Mouse, pNestin-CreER^{T2}	Jackson Laboratory	016261; RRID:IMSR_JAX:016261
Mouse, Rosa26-CAG-loxP-stop-loxP(LSL)-GCamP3	Jackson Laboratory	014538; RRID:IMSR_JAX:014538
Mouse, Rosa26-CAG-LSL-eNpH3.0-YFP	Jackson Laboratory	024109; RRID:IMSR_JAX:024109
Mouse, Rosa-LSL-tdTomato	Jackson Laboratory	007914; RRID:IMSR_JAX:007914
Mouse, Rosa26-CAG-LSL-ChR2(H134R)-YFP	Jackson Laboratory	024109; RRID:IMSR_JAX:024109
Oligonucleotide Primers		
Cre-forward: CATCTGCCACCAGCCAGCTATCAACTCG	This paper	N/A
ERT2-reverse: ACTGAAGGGTCTGGTAGGATCATACTCG	This paper	N/A
GC-forward: TGGGGATGGTCAGGTAAACT	This paper	N/A
GC-reverse: CCACATAGCGTAAAAGGAGCA	This paper	N/A
ChR-forward: TCTGCCTGGGTCTGTGTTATGGTGC	This paper	N/A
ChR-reverse: TGGTCTTGCGAATGTCGCCGTGG	This paper	N/A
Halo-forward: TGGATGTTCCATCTGCTTCTG	This paper	N/A
YFP-reverse: TTGCCGGTGGTGCAGATGAA	This paper	N/A
td-forward: CCGCCAAGCTGAAGGTGACCAAG	This paper	N/A
td-reverse: TGGATCTCGCCCTTCAGCAC	This paper	N/A
Imaging and Sleep Recording		
Microendoscope lens (1-mm diameter, 4-mm length)	Inscopix	1050-002176
Teflon-coated wires	Cooner Wire	AS633
Miniaturized microendoscope camera	Inscopix	nVista
Optic ferrule (200-μm diameter)	Thorlabs	CFLC230
Fiberoptic Rotary Joint	Doric Lenses	FRJ_1x2i_FC-2SMA_0.22
RNaseq		
O.C.T. compound	Sakura Finetek	4583
TRIzol reagent	Thermo Fisher Scientific	15596026
SMARTer Stranded Total RNA Sample Prep Kit	Takara	Z4873N
CLC Genomics Workbench	QIAGEN	v10.1.1
BedTools	Quinlan and Hall, 2010	v2.25.0, https://doi.org/10.1093/bioinformatics/btq033

(*Continued on next page*)

Continued

REAGENT/RESOURCE	SOURCE	IDENTIFIER(S)
Other Software and Algorithms		
Mosaic	Inscopix	V1.2
MATLAB	Mathworks	R2017b
CNMF-E package	FOOPSI	AR1 model
IgorPro 8	Wavematrics	version 8.01B01
Vital recorder	KISSEI COMTEC	Vital recorder2
LabChart	AD Instruments	Ver7
TimeFZ	O'HARA & CO., LTD.	TimeFZ4
Freezeframe	Med Associates	Version 4.104
Spiso-3D	Mukai et al., 2011	https://doi.org/10.1093/cercor/bhr059
GraphPad Prism	GraphPad Software	7.04 for Windows
Other Chemicals		
Tamoxifen	Merck	T5648
Sunflower Oil	Wako	196-15265
Lucifer Yellow	Thermo Fisher Scientific K.K.	L453

RESOURCE AVAILABILITY

Lead Contact

Further information and requests for resources and datasets should be directed to and will be fulfilled by the Lead Contact, Masanori Sakaguchi (sakaguchi.masa.fp@alumni.tsukuba.ac.jp).

Materials Availability

All unique/stable reagents generated in this study are available from the Lead Contact with a completed Materials Transfer Agreement.

Data and Code Availability

Data underlying the results described in this manuscript, except raw data for RNA analysis, are available at Mendeley Data: [https://doi.org/10.17632/gfbdv5kfrz.1]: https://data.mendeley.com/datasets/gfbdv5kfrz/draft?a=fee1e084-7cd0-479b-99fc-a59a4cf1f7ab

RNaseq raw data are available at Mendeley Data: [https://doi.org/10.17632/pfgkv43yn7.1]: https://data.mendeley.com/datasets/pfgkv43yn7/draft?a=a45e0f20-86a1-4306-a286-353f863d3e46

EXPERIMENTAL MODEL AND SUBJECT DETAILS

All animal experiments were approved by the University of Tsukuba Institutional Animal Care and Use Committee. Mice were maintained in a home cage (cylindrical Plexiglas cage: 21.9-cm diameter, 31.6-cm height) in an insulated chamber (45.7 × 50.8 × 85.4 cm), which was maintained at an ambient temperature of 23.5 ± 2.0°C under a 12-h light/dark cycle (9 am to 9 pm) with *ad libitum* access to food and water in accordance with institutional guidelines.

Mice (Jackson Laboratory) harboring pNestin-CreER^{T2} (nestin mice, stock #016261), Rosa26-pCAG-loxP-stop-loxP(LSL)-GCaMP3 (GC mice, Ai38, stock #014538), Rosa26-pCAG-LSL-eNpH3.0-YFP (Halo mice, Ai39, stock #014539), Rosa26-pCAG-LSL-channelrhodpsin-2-YFP (ChR mice, Ai32, stock #024109), or Rosa-pCAG-LSL-tdTomato (tdTomato mice, Ai14, stock #07914) were backcrossed in a C57BL6/J background more than 10 times. Nestin$^{+/WT}$ mice were bred with Halo$^{+/+}$ mice, resulting in F1 Halo^{nestin} and Halo^{WT} offspring at a nearly 1:1 ratio. We used a similar method to create ChR^{nestin}, GC^{nestin}, and tdTomato^{nestin} mice. All transgenes in F1 mice were kept as heterozygotes in the chromosome used for the experiments (but not for breeding) to avoid possible complications of overexpressing Cre recombinase (Forni et al., 2006) or loss of the Rosa allele (Zambrowicz et al., 1997). Only male F1 mice were used. Mice were group-housed 2-5 per cage before surgery and habituated to experimenter handling by two or three 2-min handling sessions/day for a total of 11 sessions before behavioral experiments. Age-matched littermates were always used to compare Halo^{WT} versus Halo^{nestin} and ChR^{WT} versus ChR^{nestin} to avoid potential confounds of litter, age, cage, tamoxifen administration, or light delivery. In this manner, the only difference between genotypes of mice was the presence of Cre. Genotypes of Halo and ChR mice used in the experiments were reconfirmed by tail genotyping or the presence of fluorescence signals in ABNs after completion of experiments.

Primers used were as follows: For nestin mice, Cre-forward: CATCTGCCACCAGCCAGCTATCAACTCG, ERT2-reverse: ACTGAAGGGTCTGGTAGGATCATACTCG; successful PCR amplification produced a 430-bp band. For GC mice, GC-forward: TGGGGATGGTCAGGTAAACT, GC-reverse: CCACATAGCGTAAAAGGAGCA; successful PCR amplification produced a 226-bp band. For ChR mice, ChR-forward: TCTGCCTGGGTCTGTGTTATGGTGC, ChR-reverse: TGGTCTTGCGAATGTCGCCGTGG; successful PCR amplification produced a 321-bp band. For Halo mice, Halo-forward: TGGATGTTCCATCTGCTTCTG, YFP-reverse: TTGCCGGTGGTGCAGATGAA; successful PCR amplification produced a 700-bp band. For tdTomato mice, td-forward: CCGCCAAGCTGAAGGTGACCAAG, td-reverse: TGGATCTCGCCCTTCAGCAC; successful PCR amplification produced a 320-bp band.

METHOD DETAILS

Tamoxifen injection

To induce transgene expression (i.e., GC, tdTomato, ChR, Halo) in ABNs, all F1 mice were treated with tamoxifen at 7 weeks of age by experimenters who were blind to genotype. This design ensured that the target neurons were from the same neural/stem progenitor pool and that phenotypic differences between mice were not attributed to nonspecific tamoxifen effects. Tamoxifen (120 mg/kg) was injected into the peritoneal cavity five times at 1- or 2-day intervals, with completion of the injection period within 10 days. To prepare tamoxifen solution, 30 mg tamoxifen (T5648, Merck, USA) was dissolved in 100 μl of 100% EtOH. Next, 1,000 μl sunflower oil (Wako, Japan) was added and placed in an ultrasonic cleaner for further dissolution. In the last step, ethanol was evaporated by a centrifuge.

Implantation of lens and EEG/EMG electrodes

At 9 weeks of age, mice were anaesthetized with isoflurane and fixed in a stereotaxic frame (Stoelting, USA). The height of bregma and lambda were adjusted to be equal. The microendoscope lens (1-mm diameter, 4-mm length, Inscopix, USA) was placed at anterior-posterior (AP) −2.0 mm, medial-lateral (ML) +1.2 mm, and dorsal-ventral (DV) −1.95 mm. After implanting the lens, EEG/EMG electrodes were placed (Kumar et al., 2015) (Figure S4A). Briefly, EEG electrodes were stainless steel recording screws implanted epidurally at AP +1.5 mm and −3 mm and ML −1.7 mm, and EMG electrodes were stainless steel Teflon-coated wires (AS633, Cooner Wire, USA) bilaterally placed into the trapezius muscles. One week after electrode placement, the baseplate for a miniaturized microendoscope camera (nVista, Inscopix, USA) was attached above the implanted microendoscope lens. After baseplate surgery, mice were habituated to the attached microendoscope camera for 7-8 days before recording. After completion of each experiment, randomly chosen mice were subject to histological analysis to confirm the location of the lens in the brain.

Ca^{2+} imaging and data analysis

We tested several versions of GCaMP including GCaMP3, 6 s, 6f, 7f, and 8, but only GCaMP3 showed consistent expression in young ABNs in nestin mice; thus, this version was used. All Ca^{2+} imaging was performed at 11 weeks of age. For the 4-h recordings shown in Figure 1D, imaging started at zeitgeber time (ZT) = 1. For experiments involving foot shocks shown in Figures 1E–1H and S5C, the recording duration was 2-3 h and began immediately after mice were returned to the home cage, which was around ZT = 1 or 4. For baseline recordings, a recording period of 2-3 h during an equivalent circadian time period occurred on the previous day in the same mice. For longitudinal recording over the course of the behavioral protocol shown in Figures 1I–1K, the recording started at ZT = ∼0.

For Ca^{2+} trace extraction by experimenters who were blind to mouse group, recordings were spatially down-sampled at 5.02 Hz and motion-corrected in Mosaic v1.2 (Inscopix). Fluorescence traces from single neurons were extracted in MATLAB using constrained non-negative matrix factorization for microendoscopic data (CNMF-E) (Zhou et al., 2018). Raw video was filtered using a mean-subtracted 2D Gaussian kernel resembling average neuron diameters (gSig = 4, gSiz = 12). Seed pixels were initialized with a greedy model considering a minimum local correlation of 0.7 and a minimum peak-to-noise ratio (PNR) of 6. Local background was corrected with a ring model (radius = 25). False cell detection, cell merging, and motion artifacts were verified by visual inspection of neuron shape and temporal dynamics of Ca^{2+} transients. To detect significant Ca^{2+} transients, a 200^{th}-order median filter was used to remove slow Ca^{2+} fluctuations not related to fast Ca^{2+} transients (e.g., slow variation in the internal storage of Ca^{2+} that may hinder the proper extraction of Ca^{2+} transients). Signal was deconvolved using the CNMF-E package (FOOPSI, AR1 model). To reduce the number of false positives, we constrained Ca^{2+} transients to be $\geq$ 5 standard deviations from the remnant of the deconvolved Ca^{2+} signals (see Figure S3 for details). Raster plots and sleep stage matching were performed in IgorPro 8 (Wavemetrics). The timing of a Ca^{2+} transient was estimated at the time of its peak. Fluorescence trace amplitudes are reported relative to the level of noise.

Average Ca^{2+} transient rate by event probability

The harmonic mean (Figure S3B, the inverse of the average inter-event interval) is widely used for rate estimation, including that of Ca^{2+} transients. However, the harmonic mean may not be suitable for representing the slow rate of ABN Ca^{2+} transients. This is because each wake or sleep episode can be as short as 10 s, whereas the Ca^{2+} transient rate is on the order of 1 event/min, making it impossible to obtain a precise inter-event interval. Therefore, we examined the use of event probability to calculate the rate of ABN Ca^{2+} transients (Figure S3C). Event probability was calculated by dividing the total number of Ca^{2+} transients by the total recording time for all cells in each experimental group. To compare the use of event probability versus harmonic mean to calculate Ca^{2+} transient rate in REM sleep (as it has the shortest episode duration on average compared with that of NREM and wakefulness), we plotted

the rate calculated by both methods (Figure S3D, y axis) against simulated events (Figure S3D, x axis). We first simulated events generated according to a Poisson point process. Next, we obtained the distribution of REM episode durations from our experimental data, from which we created pseudorandom REM episodes. Finally, we calculated the Ca^{2+} transient rate in each episode. Using this probability, we found that the harmonic mean tended to overestimate the Ca^{2+} transient rate at < 0.02 events/s, which is higher than that previously reported in ABNs during wakefulness (Danielson et al., 2016). Therefore, we used the event probability method to calculate ABN Ca^{2+} transient rate.

We calculated confidence interval (CI) for Ca^{2+} transient rate using a bootstrap method in which we estimated the distribution of the mean rate by resampling with random replacement of cells (Figure S3E) (bootstrap resamples). This was repeated 10,000 times to obtain a 95% CI (Figure S3F). To determine the mean difference between two groups, the CI of the difference between groups was calculated. For multiple comparisons, statistical significance was corrected by the Bonferroni method.

Calculation of Ca^{2+} transients for 4 h

Due to the limits of our system for handling large amounts of image data (Windows 10 professional with 128GB RAM), we split each 4-h movie file into two shorter files (2 h each) for further processing and duplicated the above-described Ca^{2+} transient extraction process for each mouse (total of 8 separated files from 4 mice). To detect the same cells in the two separated files for Figures S4B and S4C, we used a previously described algorithm (Sheintuch et al., 2017).

Imaging ABN activity across the behavioral protocol

We used the same GC^{nestin} mice and DS protocol, with a few modifications, to examine the likelihood of young ABNs being active across different contextual fear conditioning and testing periods. In a preliminary experiment, we noticed that microendoscope attachment reduced freezing behavior, seemingly due to its weight. Therefore, we performed 6 days of habituation to microendoscope attachment before contextual fear conditioning, which resulted in low but context-specific freezing (Figure S4S). On the conditioning day, we attached the microendoscope to mice at ZT = ~0 and performed Ca^{2+} recording for 10 min in the home cage and an additional 10 min in context A before the shock during conditioning, creating a single "Pre-shock" recording file for each mouse. We then detached the microendoscope (< 1 min) to avoid a change in the field of view due to hitting the microendoscope against the wall during the shock, performed the DS protocol as described above in context A, re-attached the microendoscope (< 1 min), and performed 5 min of recording after the shock in context A, creating a "Post-shock" recording file for each mouse. Subsequently, we performed 2.5 h of recording toward the latter part of the 5.5-h consolidation period in the home cage (covering most of the REM sleep episodes within the period of our image processing capability as described above) and 10 min of recording during the memory retrieval test in context A without stopping the recording, creating a single "Consolidation-Test" recording file for each mouse. The time gap between the end of the Post-shock period and the start of the 2.5-h recording window was 3 h 2 m ± 0 h 1 m (mean ± SEM) and between the end of the 2.5-h recording window and the start of the Test was 7 m ± 1 m (mean ± SEM). Some mice were assigned to a no-shock control group (i.e., DS protocol without shocks), and other mice underwent DS conditioning in context A followed 3 h later by a 5-min session in context C. Context C consisted of a circular glass chamber (22-cm diameter) with a floor covered with paper and no ethanol odor.

Tracking same cells across the behavioral protocol

To identify and track the same neurons within multiple imaging files across different behavioral settings (Figures 1I–1K), we concatenated the Pre-shock, Post-shock, and Consolidation-Test files into a single file. Then, we identified neurons from the concatenated file (Ghandour et al., 2019; Jimenez et al., 2018) using the multi-batch implementation of CNMF-E, which is optimized for analyzing multiple recordings, allowing us to project the same neuronal footprints across the file (Zhou et al., 2018).

To confirm that we tracked the same neurons across the concatenated file, we compared the footprints of identified neurons using separate files as previously described (Ghandour et al., 2019; Gonzalez et al., 2019; Jimenez et al., 2018). We chose to compare Pre-shock and Post-shock files because this is where the largest misalignment between files could have occurred due to disconnecting the microendoscope between the two recording sessions (Gonzalez et al., 2019). The spatial footprints of the identified neurons of the Pre-shock and Post-shock periods were almost identical in the two separate files (Figure S3G) and the concatenated file (Figure S3H).

Importantly, some neurons were detected in only one separate file (Figure S3I, green/red trace), which could lead to the misinterpretation of some neurons as inactive in some periods. However, these neurons displayed significant Ca^{2+} transients during the periods extracted from the concatenated file (Figure S3I, gray trace). This can occur when the local correlation or PNR of the pixels falls below the threshold defined in CNMF-E when separate files are used. This issue is especially relevant to the experiment shown in Figures 1I–1K, as the two recording files were only 5 min (Post-shock) and 20 min (Pre-shock) in duration, whereas ABN activity is sparse (< 0.5 event/min) and not normally distributed.

Moreover, we found that the spatial component extracted from the concatenated file showed single round-shaped cells exhibiting similar amplitudes and shapes of Ca^{2+} transients across different behavioral settings (Figure S3J, left). The time component demonstrates truly silent neurons in some contexts, evidenced by their absence of Ca^{2+} transients (Figure S3J, right).

We next systematically evaluated the accuracy of our cell tracking. As the local correlation and PNR images are used to initialize spatial footprints in the CNMF-E algorithm, we created images (Figure S3K, top) by multiplying the local correlation and PNR of each

target period from the concatenated file as previously described (Zhou et al., 2018). By thresholding these images with the parameter used to detect neurons, we obtained spatial masks (Figure 3K, bottom) showing several coactive regions in target periods, reflecting neuronal activities. Theoretically, the maximum similarity between the spatial masks of any two periods can be achieved when they are perfectly aligned. Thus, we calculated a similarity score defined as the cosine similarity between the spatial mask vectors divided by the cosine similarity obtained from their best alignment (Pnevmatikakis and Giovannucci, 2017). To test the performance of this approach, we divided the Pre-shock period images into two halves and systematically introduced pixel misalignments in eight directions to the second half. As expected, this resulted in a monotonic decrease in similarity score between the two halves with increasing pixel misalignment (Figure S3L). Importantly, the 5-pixel misalignment equals the minimum distance between two neurons defined in the CNMF-E configuration, which may lead to neural duplications (i.e., merging threshold), resulting in a similarity score of ~0.4.

Finally, we examined similarity scores at the three most vulnerable points: (1) Pre-shock versus Post-shock (i.e., removal of the microendoscope), (2) Post-shock versus Consolidation-Test (i.e., long duration (~3 h) between recording sessions), and (3) 1st quartile versus 4th quartile of Consolidation-Test (i.e., long, continuous duration (> 2.6 h) of a single recording session). All three comparisons showed similarity scores > 0.95 (Figure S3L, inset). To further confirm stable identification of the same cells within long, continuous recording sessions, we examined similarity scores between quartiles throughout the Consolidation-Test period, which were consistently > 0.95 (Figure S3M). Taken together, these results provide evidence of our capability to track the same neurons throughout the behavioral protocol.

Slice patch clamping

Coronal brain slices from 11-week-old Halo^{nestin} mice that received five tamoxifen injections were prepared as previously described (Willadt et al., 2014). Current injection was performed with a patch clamp electrode at the soma. Orange light delivery was used to stimulate Halo. Laser light was focused into the back focal plane of a LUMPLAN 40 × lens and exited as a parallel beam. The diameter and total area of the illuminated area was 1 mm and 0.78 mm^2, respectively. Light power density was 66 mW/cm^2.

Optic cannula and electrode implantation

At 8 (Figures 6L and 6M), 10, or 16 weeks (Figures 6N and 6O) of age, mice were anaesthetized with isoflurane and fixed in a stereotaxic frame by experimenters who were blind to mouse genotype. The height of bregma and lambda were adjusted to be equal. Optic cannulas (200-μm diameter, 5-mm length optic fiber plus zirconia connector, Thorlabs, Japan) were placed at AP −2.00 mm, ML ± 1.10 mm, and DV −1.95 mm (Figure S6). For DG LFP recordings, an unsheathed portion of platinum wire was attached to the tip of the optic fiber. After optic cannula implantation, electrodes were placed as described above. Mice were habituated to being chronically tethered in the recording chamber for 7-8 days until they exhibited a regular sleep-wake cycle. After completion of each experiment, randomly chosen mice were subject to histological analysis to confirm the location of the optic cannulas in the brain.

EEG/EMG/LFP recording

Before behavioral experiments, mice underwent baseline EEG/EMG/LFP recording in their home cage equipped with a data acquisition system (LabChart, AD Instruments, New Zealand for GC^{nestin} mice; Vital recorder, KISSEI COMTEC, Japan for other mice). EEG/EMG/LFP signals were recorded during BL and AS periods for each mouse. EEG/EMG/LFP data were collected at a sampling rate of 100 Hz for GC^{nestin} mice and 128 Hz for other mice. Coaxial electric and optic (Doric Lenses, Canada) slip rings allowed mice to move and sleep naturally.

Sleep stage analysis

Real-time vigilance state analysis was conducted based on visual characteristics of EEG and EMG waveforms with consistent timing indicators on the display for wave frequency determination and video surveillance of mouse movement by experimenters blind to mouse genotype. Wakefulness was defined by continuous mouse movement or de-synchronized low-amplitude EEG with tonic EMG activity. NREM sleep was defined by dominant high-amplitude, low-frequency delta waves (1-4 Hz) accompanied by less EMG activity than that observed during wakefulness. REM sleep was defined as dominant theta rhythm (6-9 Hz), and the absence of tonic muscle activity. Based on sleep state judgement, the operator controlled the pulse generator, which was connected to the laser controller (see Table S1 for verification of the timing of light delivery). 470-nm blue and 590-nm orange lasers (Shanghai Lasers, China, 20 mW fiber output at the tip of the optic cannula) were used to stimulate ChR2 and Halo, respectively. The generators produced 0.05-Hz transistor-transistor logic pulses (10 s on/off cycles) for the orange laser and 20-Hz pulses (25-ms on/off cycles) for the blue laser. Offline sleep architecture analysis and Fast Fourier Transform analysis were performed using Sleep Sign software (KISSEI COMTEC) based on the above criteria. If a 10 s epoch contained more than one sleep state (NREM sleep, REM sleep, or wakefulness), the most represented state was assigned for the epoch (Kumar et al., 2015).

Duration and timing of light delivery

The total duration of silencing, on average, was 11 min during REM sleep, 105 min during NREM sleep, and 21 min during wakefulness. The sensitivity and accuracy of light delivery procedures were calculated by comparing online and offline judgements of sleep state. Briefly, we first subdivided the 6-h time window of light intervention into 10 s epochs offline and classified each epoch into true

positive (TP: the light was correctly on), false positive (FP: incorrectly on), false negative (FN: incorrectly off), or true negative (TN: correctly off) categories (Table S1). Two measures were calculated as follows:

$$\text{Sensitivity} = \text{TP}/(\text{TP} + \text{FN})$$

$$\text{Accuracy} = (\text{TP} + \text{TN})/(\text{TP} + \text{FP} + \text{FN} + \text{TN})$$

Affected number of Ca^{2+} transients by silencing

The absolute number of Ca^{2+} transients observed during imaging cannot be compared to the extent of optogenetic silencing for two reasons. First, the effective area differs between imaging and optogenetic intervention (Figure 3C); the lens for Ca^{2+} imaging has a focal plane, but optogenetic intervention does not. Second, the imaging experiment only recorded Ca^{2+} signals from ABN cell bodies. However, optogenetic intervention impacts not only cell bodies but also spines, dendrites, and axons. Notably, ABN axons form a bundle-like structure (i.e., mossy fiber pathway) that takes an orthogonal path toward the CA3, passing through the illuminated region. Statistically speaking, the Ca^{2+} transients of ABNs during REM sleep are not randomly distributed, and the total REM duration within the 6 h of optogenetic intervention extends to 22.2 min on average (Figure 3D). These factors were considered to estimate the affected number of ABNs by optogenetic stimulation.

Calculating auto-correlation values

We subdivided all REM sleep episodes within 6 h after contextual fear conditioning into 10 s epochs from DG LFP recordings. Epochs < 10 s were ignored. A total of 902 sets of time series (10 s epochs) were generated. For each time series, we calculated the auto-correlation function as

$$C(\tau) = \frac{\langle x(t)x(t+\tau)\rangle - \langle x(t)\rangle^2}{\langle x(t)^2\rangle - \langle x(t)\rangle^2}$$

where x(t) is the local field potential at time t, τ is time lag (s), and $< \ldots >$ denotes the average over the entire length of the time series. We obtained τ_{max} values at which the auto-correlation was maximal (i.e., max corr. value) within the first and second negative peaks.

Spine analysis

Due to the necessity of visually identifying ABNs (by YFP signal) to inject the tracer dye for analyzing spines in control groups, we used $Halo^{nestin}$ mice with no light delivery and ChR^{nestin} mice with orange light (590 nm) delivery, which does not activate ChR2 (Han et al., 2009). $Halo^{nestin}$ and ChR^{nestin} mice underwent IS or DS conditioning at ZT = 2, after which orange light was delivered to ABNs in REM sleep during a 6-h period (except for in the no light group) with experimenters blind to mouse genotype. At ZT = 8, mice were deeply anesthetized with isoflurane and decapitated. Immediately after decapitation, the brain was removed from the skull and placed in ice-cold oxygenated (95% O_2, 5% CO_2) artificial cerebrospinal fluid (ACSF) containing (in mM): 124 NaCl, 5 KCl, 1.25 NaH_2PO_4, 2 $MgSO_4$, 2 $CaCl_2$, 22 $NaHCO_3$, and 10 D-glucose; pH was 7.4. The hippocampus was dissected, and 200-μm slices transverse to the long axis from the middle third of the hippocampus were cut using a vibratome (Leica). Hippocampal slices were transferred to an incubation chamber containing ACSF held at 25°C for 2 h to allow slice recovery. Slices were then prefixed with 4% paraformaldehyde (PFA) at 4°C overnight. ABNs within slices were visualized by injection of Lucifer Yellow (Duan et al., 2002) (Thermo Fisher Scientific K.K., Japan) and an Olympus EX51WI microscope (Olympus, Japan) equipped with a STC-TB33USB-AS CCD camera (OMRON SENTECH, Japan) and 60 × water immersion lens (Olympus). Under the visual guidance of YFP signal, ABNs were selectively injected with a glass electrode with a tip filled with 5% Lucifer Yellow for 15 min using Axopatch 200A (Axon Instruments, USA). Neurons within a 100-μm depth from the surface of a slice were injected.

Fear conditioning

As the experiments were conducted at two different facilities, we used two similar but slightly different fear conditioning contexts: one (Kishimoto et al., 2015) for GC^{nestin} mice and another (Purple et al., 2017) for other mice. For GC^{nestin} mice, the conditioning chamber consisted of clear acrylic walls and a stainless steel grid floor (width × depth × height, 310 × 250 × 280 mm; O'Hara and Co., Japan). The grid floor had bars (2.0-mm diameter) spaced 6.0 mm apart allowing the delivery of electric shocks. A white acrylic drop pan under the grid floor was cleaned with 75% ethanol, which also provided a background odor. The conditioning chamber was placed inside an isolated behavioral chamber to keep the visual and sensory cues constant. A camera was placed at the top of the behavioral chamber and was remotely controlled so that mice could not see the experimenter during context exposure. The same context was used for the DS and IS experiments. For other mice, a metal conditioning chamber contained a stainless steel grid floor (310 × 240 × 210 mm; MED Associates, USA). The grid floor consisted of bars (3.2-mm diameter) spaced 7.9 mm apart allowing the delivery of electric shocks. A stainless steel drop pan under the grid floor was also cleaned with 75% ethanol. The front, top, and back of

the chamber were made of clear acrylic, and the two sides were made of aluminum panels. The visual and sensory cues were kept constant. A camera was placed at the back of the chamber and was remotely controlled so that mice could not see the experimenters during context exposure.

One day after the baseline recording session in the sleep chamber, mice underwent contextual fear conditioning around ZT = 1 or 4 for GC^{nestin} mice or ZT = 2 for $Halo^{nestin}$ and ChR^{nestin} mice by experimenters blind to mouse genotype. Mice in both the DS and IS groups received three electrical foot shocks (0.75 mA, 2 s) during a 360 s session. In the DS group, mice received a shock 148, 238, and 328 s after being placed in the context and were returned to their home cages 30 s after the last shock. In the IS group, mice received a shock 0, 4, and 8 s after being placed in the context and were returned to their home cages at the end of the 360 s session.

After conditioning, mice underwent Ca^{2+} imaging or light delivery sessions (except for in the no light group) in their sleep chamber by experimenters blind to mouse genotype. At the same of the conditioning on the next day, mice were placed in the conditioning context for 5 min. Freezing behavior was used as an index of contextual fear memory. Freezing behavior was measured using an automated scoring system (Ohara system for GC^{nestin} mice or Freezeframe (Med Associates) for other mice) and was defined as a $\geq$ 1 s continuous absence of movements except for breathing. Shock reactivity was calculated for each mouse by comparing its movement during the 2 s of the first shock and 2 s immediately before the first shock (Figures 6G and 6H).

For auditory fear conditioning, mice were placed in the conditioning context (context A) for 360 s in total, and three tones (30 s each, 2800 Hz, 85 dB) were played at 120, 210, and 300 s, with each tone co-terminating with a 2 s foot shock (0.75 mA). During the memory test, mice were placed in a non-conditioned context (context B) for 360 s in total, and the tone was played during the last 180 s of the session. Context B was similar to the conditioning context except that the floor and sides of the chamber were covered with white plastic sheets, a piece of cardboard with a blue and white rectangular pattern was affixed to the back wall, and ethanol was not used for cleaning.

Confocal microscopy and morphological analysis

In vitro imaging analysis was performed from sequential *z*-series scans with a Leica TCS SP8+ confocal microscope (Leica, Germany). For analysis of spines, 3D images were constructed from approximately 20 sequential *z*-series sections of neurons scanned every 0.45 μm with a 63 × oil immersion lens (Leica). Confocal images were deconvoluted using Hyvolution software (Leica). Spine density, head diameter, and neck length were measured with Spiso-3D software (Mukai et al., 2011). Spine density was calculated from the number of spines in the field of view, which contained a 40- to 55-μm portion of a dendrite. We focused on analyzing dendrites within the outer molecular layer located 80-120 μm from the soma (Hojo et al., 2015). Within this portion of dendrites, granule neurons mainly receive excitatory synaptic inputs from the lateral and medial entorhinal cortex through the perforant path (Dolorfo and Amaral, 1998). Spines were defined as protrusions from the dendritic stalk with a rounded head region. Spine neck length was determined using coordinates for centers of the spine head and dendrite. The overlap between NeuN and tdTomato signals was confirmed in 1-μm optical sections of the DG upper blade in the dorsal hippocampus using a 40 × oil lens.

WGA labeling

WGAcre fragment was synthesized from pAAV-EF1a-mCherry-IRES-WGACre (a gift from Dr. Karl Deisseroth, Stanford University) and cloned into retrovirus by replacing the GFP-expressing cassette in the pCAG vector (#49054, Addgene, USA). The original plasmid was used to create GFP-expressing virus for control experiments. The transgene was packaged into moloney murine leukemia virus (MMLv) with a titer of approximately 2×10^9 transfection units/ml (GT3 Core Facility, Salk Institute), similar to previous described procedures (Tiscornia et al., 2006) except that only gag-pol and env (VSV-G) helper plasmids were used. Hemizygous tdTomato mice at 6-8 weeks of age were used for stereotaxic injection to target ABNs (AP −2.0 and −2.7, ML ± 1.55 and ± 2.0, DV −2.0 and −2.25) with 1 μl MMLv at each site. Mice were perfused 2 or 4 weeks post-infection for analysis. Imaging and quantification of tdTomato-expressing neurons were performed using a microscope (Imager M2, Zeiss) with 10 × and 20 × lenses.

Immunohistochemistry

Mice were perfused transcardially with PBS (0.1 M) and 4% PFA. Brains were removed, fixed overnight in PFA, and transferred to PBS. Coronal sections (40 μm) were cut using a vibratome (VT1200S, Leica). Sections were incubated overnight with mouse monoclonal anti-NeuN (1:1,000; Millipore), goat polyclonal anti-Dcx (1:200; Santa Cruz Biotechnology), and/or rabbit polyclonal anti-GFP (1:8,000; Thermo Fisher) primary antibodies and for 60 min at 20°C with Alexa Fluor- or biotin-conjugated secondary antibody (1:750; Jackson Immunoresearch Laboratories, USA). An ABC kit (Vector, USA) and TSA reaction were used for signal amplification for Dcx staining. Sections were mounted on slides with mounting medium containing DAPI (Merck).

Transcriptome analysis

After contextual fear conditioning and silencing of young ABNs during REM sleep (ZT = 2-8), brain samples were obtained at ZT = 8 (5 pm). Mice were sacrificed by cervical dislocation, and brains were immediately removed from the skull and frozen at −80°C in OCT compound (Sakura Finetek USA). Five coronal sections (10 μm) around AP −2.00 mm containing the DG were prepared. After methanol fixation, hematoxylin staining, and dehydration by ethanol, the upper blades of the DG were obtained by laser microdissection (LMD-6000, Leica). For isolation of total RNA, 160 μl Trizol reagent (Thermo Fisher Scientific) was added to tissue pieces isolated by LMD and processed according to the manufacturer's instructions except that isolation was performed in 200-μl PCR tubes until

phase separation. RNA yield and degradation status were monitored by a Bioanalyzer RNA Pico chip (Agilent Technologies). Total RNA samples (484-3,484 pg) were directly used as input for library synthesis using the SMARTer Stranded Total RNA Sample Prep Kit (Takara). Sequencing libraries were quantified by a DNA High-Sensitivity chip (Agilent Technologies). 2 × 36-base sequencing was performed by Illumina NextSeq500 (Illumina) at Tsukuba i-Laboratory LLP.

Sequencing read FASTQ files were imported to CLC Genomics Workbench (v10.1.1, QIAGEN) and mapped to the mm10 mouse genome. Total counts were obtained for 49,585 genes. Data were analyzed using Empirical Analysis in the DGE tool after removal of genes with maximum counts < 30 across all samples (n = 8), which left 11,170 genes. Differentially expressed genes (n = 9) were defined as having an FDR corrected $p < 0.05$ and $|\text{fold change}| > 2$. To visualize RNA sequencing reads, mapped tags were exported from CLC Genomics Workbench as BAM files, converted into bedgraph files using BedTools (v2.25.0), and visualized using the USCS Genome Browser. For promoter motif analysis, coordinates of 200-bp upstream and 100-bp downstream regions of transcription start sites were created based on RefSeq database records and defined as promoter regions. Promoter regions for filtered up- or downregulated genes were obtained and converted into nucleotide sequences as FASTA files. These sequences were analyzed using the DRMEME tool (http://meme-suite.org/), and results were used as input for TOMTOM to find enriched motif and corresponding transcription factor candidates. Pathway analysis was performed using the Metascape webtool (https://metascape.org/gp/index.html#/main/step1).

Granule neuron labeling, imaging, and manipulation

We used the same volume (180 nl) of AAV:CaMKII-Cre vector from only one preparation (i.e., single batch) and the same duration between virus injection and imaging/optogenetic manipulation (26 days) across all AAV experiments.

AAV vector was prepared as previously described (Lazarus et al., 2011). Briefly, AAV was generated by tripartite calcium phosphate transfection (AAV-1 expression plasmid, Penn Vector Core), adenovirus helper plasmid (Agilent), and pAAV plasmid pENN.AAV.CamKII 0.4.Cre.SV40 (#105558, Addgene, USA) into 293A cells. After 3 days in 5% CO_2 at 37°C, 293A cells were re-suspended in artificial cerebrospinal fluid, frozen and thawed four times, and treated with benzonase nuclease (Millipore, ref. #E1014) to degrade all forms of DNA and RNA. Cell debris were removed by centrifugation, and the virus titer in the supernatant was determined using real-time polymerase chain reaction ($> 1 \times 10^{13}$ viral genome/ml).

Virus injection was performed as previously described (Lazarus et al., 2011). Briefly, adult mice (~8-week-old GC mice or ~9-week-old Halo mice) were anesthetized with isoflurane and fixed in a stereotaxic frame (Stoelting, USA). AAV solution was injected into the dorsal hippocampus at AP 2.0 mm, ML ~1.5 mm, and DV 1.5 mm relative to bregma. Virus was injected using a picospritzer III air pressure-based injection system (S48 Stumilator, Grass Technologies, USA) connected to a glass pipet injector. Injections were performed slowly over 15 min. After microinjection, the injector needle was left in place for 5 min and then slowly withdrawn. Mice were allowed to recover for 1 week before lens implantation (and then another 1 week after baseplate implantation) or 2 weeks for the silencing experiments.

QUANTIFICATION AND STATISTICAL ANALYSIS

Statistical analysis was performed using GraphPad Prism version 7.04 for Windows (GraphPad Software, USA) or Igor Pro version 8.01B01 (Wave Metrics, USA). Type I error was set at 0.05. Shapiro-Wilk tests were performed to assess the normality of data. Brown-Forsythe tests were performed to assess homogeneity of variance. Other details of statistical analyses are described in the figure legends and below.

Figure 1D. NREM versus Wake: bootstrap with Bonferroni correction, $p < 0.05$ for 1 h, 2 h, 3 h, and 4 h. REM versus NREM: bootstrap with Bonferroni correction, $p < 0.05$ for 1 h. Wake versus REM: bootstrap with Bonferroni correction, $p < 0.05$ for 1 h, 2 h, 3 h, and 4 h.

Figure 1F. DS (n = 14) versus IS (n = 17), $t(25) = 6.0$, Welch corrected, $p < 0.0001$. When testing only mice used for imaging (n = 7 each), $t(12) = 2.8$, $p = 0.016$. Two-tailed unpaired t test.

Figure 1G. n = 7 mice. REM, AS versus BL: bootstrap, $p > 0.05$.

Figure 1H. n = 7 mice. REM, AS versus BL: bootstrap, $p < 0.05$.

Figure 1J. To avoid losing statistical power due to multiple comparisons and bias due to arbitrarily chosen comparisons, we compared pre-shock HC versus other time period data (six comparisons) and REM+ versus REM- data within each time period (four comparisons), resulting in a total of 10 comparisons made by bootstrap with Bonferroni corrections. Within REM-, pre-shock HC versus pre-shock A, $p = 0.086$; versus post-shock A, $p = 0.59$; versus test A, $p = 0.74$. Within REM+, pre-shock HC versus pre-shock A, $p = 0.17$; versus post-shock A, $p = 0.039$; versus test A, $p = 0.50$). For REM- versus REM+, pre-shock HC, $p = 0.36$; pre-shock A, $p = 0.35$; post-shock A, $p = 0.0051$; test A, $p = 0.98$. n = 59 and 36 neurons in REM- and REM+ groups, respectively, from 7 mice.

Figure 1K. Post-shock A: inactive versus active, n = 60 and 36 neurons, respectively, from 7 mice, bootstrap, $p < 0.01$; test A: inactive versus active, bootstrap, n = 72 and 24 neurons, respectively, from 7 mice, $p > 0.9$.

Figure 2E. Two-tailed paired t test, $t(5) = -11.7$, $p < 0.001$.

Figure 2F. Two-tailed paired t test, $t(4) = 15.4$, $p < 0.0001$.

Figure 3D–3F. See Data S1 for details of statistical analysis.

Figures 3G and 3H. Halo^{WT} (G, n = 13), Halo^{nestin} (H, n = 12). Power during BL and AS periods showed no obvious differences between Halo^{WT} and Halo^{nestin} mice as evaluated by their 95% CIs.
Figures 3J–3L. Peak auto-correlation values within the theta band: (J) Halo^{WT} (n = 434 epochs from 3 mice) and Halo^{nestin} (n = 468 epochs from 3 mice) mice (Mann-Whitney test, W = 100.150, p = 0.72). (K) Halo^{WT} mice (off, n = 205 and on, n = 229 epochs from 3 mice; Mann-Whitney test, W = 24.240, p = 0.56). (L) Halo^{nestin} mice (off, n = 225 and on, n = 243 epochs from 3 mice; Mann-Whitney test, W = 26.873, p = 0.75).
Figure 4. Please see Data S2 for the details.
Figure 5. As some groups did not show normal distributions or equal variance of spine data, we employed a bootstrap method to estimate *F*-test statistic distribution based on

$$F = \frac{\textit{Between group variance}}{\textit{Within group variance}}.$$

We first normalized all data to obtain a mean of 0 by subtracting each value from the group mean. Next, we obtained a distribution of empirical *F*-values by bootstrapping each value in the group. This was repeated 10,000 times. Finally, we examined whether the calculated *F*-values fell above 95% of the empirical *F*-value distribution. For post hoc tests, we estimated the distribution of the mean differences between two groups by resampling with random replacement of each data point. This was repeated 10,000 times to obtain a 95% CI. For multiple comparisons, statistical significance was corrected using the Bonferroni method (total 15 comparisons).

Group #1: IS/-/Halo (Halo^{nestin} mice in the IS group without light delivery), 1,481 spines, n = 30 dendrites, 18 neurons, 3 mice
Group #2: DS/-/Halo (Halo^{nestin} mice in the DS group without light delivery), 2,402 spines, n = 39 dendrites, 18 neurons, 3 mice
Group #3: DS/+/ChR (ChR^{nestin} mice in the DS group with orange light delivery), 2,529 spines, n = 40 dendrites, 15 neurons, 3 mice
Group #4: DS/+/Halo (Halo^{nestin} mice in the DS group with orange light delivery), 2,215 spines, n = 36 dendrites, 16 neurons, 3 mice
Figure S1D. Data from 2,435, 3,234, and 7,754 neurons, n = 4, 3, and 6 mice at 2, 4, and 10 weeks, respectively.

Figure 5C. One-way ANOVA with bootstrap methods, $F(3, 141) = 3.0$, $p < 0.05$; post hoc bootstrap and Bonferroni correction, $p < 0.05$ for IS/-/Halo versus DS/-/Halo, IS/-/Halo versus DS/+/ChR, and IS/-/Halo versus DS/+/Halo.
Figure 5D. One-way ANOVA, $F(3, 141) = 3.4$, $p < 0.05$; Sidak's multiple comparison tests, IS/-/Halo versus DS/-/Halo, $p < 0.05$, IS/-/Halo versus DS/+/ChR, $p = 0.055$, IS/-/Halo versus DS/+/Halo, $p < 0.05$.
Figure 5E. One-way ANOVA, $F(3, 141) = 6.0$, $p < 0.001$; Sidak's multiple comparison tests, $p < 0.05$ for IS/-/Halo versus DS/+/Halo, DS/+/ChR versus DS/+/Halo, and DS/-/Halo versus DS/+/Halo.
Figure 6B. Halo^{WT} (n = 12) versus Halo^{nestin} (n = 12): two-tailed unpaired t test, $t(22) = 0.72$, $p = 0.48$.
Figure 6D. Halo^{WT} (n = 13) versus Halo^{nestin} (n = 12): two-tailed unpaired t test, $t(23) = 2.2$, $p = 0.041$.
Figure 6F. Halo^{WT} (n = 9) versus Halo^{nestin} (n = 9), two-tailed unpaired t test, $t(16) = 0.020$, $p = 0.98$.
Figure 6H. Mouse movement 2 s before shock versus 2 s during first shock. Halo^{WT} (n = 13) versus Halo^{nestin} (n = 12), two-way ANOVA, group × time, $F(1, 23) = 1.1$, $p = 0.31$; time: $F(1, 23) = 173$, $p < 0.0001$; group, $F(1, 23) = 0.41$, $p = 0.53$.
Figure 6I. Halo^{WT} (n = 11) versus Halo^{nestin} (n = 14): two-tailed unpaired t test, $t(23) = 1.1$, $p = 0.29$.
Figure 6J. Halo^{WT} (n = 14) versus Halo^{nestin} (n = 12): two-tailed unpaired t test, $t(24) = 0.35$, $p = 0.73$.
Figure 6M. Halo^{WT} (n = 13) versus Halo^{nestin} (n = 16), two-tailed unpaired t test, $t(27) = 0.84$, $p = 0.41$.
Figure 6O. Halo^{WT} (n = 17) versus Halo^{nestin} (n = 18), two-tailed unpaired t test, $t(33) = 1.8$, $p = 0.084$.
Figure 6S. Halo^{WT} (n = 9) versus Halo^{nestin} (n = 9), two-way ANOVA, group × time, $F(5, 105) = 0.67$, $p = 0.65$; time: $F(5, 105) = 29$, $p < 0.0001$; group, $F(1,21) = 0.0028$, $p = 0.96$.
Figure 6V. ChR^{WT} (n = 12) versus ChR^{nestin} (n = 14), two-tailed unpaired t test, $t(24) = 2.1$, $p = 0.046$.
Figure S1E. Data from 775, 415, and 951 neurons, n = 3, 3, and 3 mice at 2, 4, and 10 weeks, respectively, two-tailed Pearson's correlation, $r(7) = 0.85$, $p < 0.004$.
Figure S1G. Data from 596 tdTomato+ neurons, n = 3 mice.
Figure S2I. GFP 4-week versus WGA 2-week versus WGA 4-week: Kruskal-Wallis H test, $H = 1.3$, $p = 0.55$.
Figure S4K. Wake, NREM, REM: BL versus AS, bootstrap, $p > 0.05$
Figure S4L. Two-way ANOVA, sleep stage × time: $F(2, 24) = 0.27$, $p = 0.77$; sleep stage: $F(2, 24) = 45$, $p < 0.0001$; time: $F(1,12) = 0.47$, $p = 0.50$.
Figure S4M. Two-way ANOVA, sleep stage × time: $F(2, 24) = 1.3$, $p = 0.29$; sleep stage: $F(2, 24) = 12$, $p = 0.0003$; time: $F(1,12) = 3.1$, $p = 0.10$.
Figure S4N. Two-way ANOVA, sleep stage × time: $F(2, 24) = 1.6$, $p = 0.23$; sleep stage: $F(2, 24) = 69$, $p < 0.0001$; time: $F(1,12) = 1.6$, $p = 0.23$.
Figure S4O. REM: BL versus AS (n = 31, 14 events, respectively), bootstrap, $p < 0.0005$
Figure S4P. Two-way ANOVA, sleep stage × time: $F(2, 12) = 2.1$, $p = 0.17$; sleep stage: $F(2, 12) = 40$, $p < 0.0001$; time: $F(1,6) = 1.3$, $p = 0.29$.

Figure S4Q. Two-way ANOVA, sleep stage × time: $F(2, 12) = 2.2$, $p = 0.16$; sleep stage: $F(2, 12) = 17$, $p = 0.0003$; time: $F(1,6) = 1.8$, $p = 0.23$.
Figure S4R. Two-way ANOVA, sleep stage × time: $F(2, 12) = 0.80$, $p = 0.47$; sleep stage: $F(2, 12) = 79$, $p < 0.0001$; time: $F(1,6) = 1.0$, $p = 0.35$.
Figure S4S. Test A, no-shock, n = 10 mice; test A DS, n = 7 mice; test C, DS, n = 7 mice. One-way ANOVA, $F(2, 21) = 8.3$, $p < 0.05$; Dunn's multiple comparison tests, test A no shock versus test A DS, $p < 0.05$, test A DS versus test C DS, $p < 0.05$.
Figure S4T. P(post-shock A ∩ test A) / (P(post-shock A) × P(test A)): REM+ versus REM-, n = 59 and 36 neurons, respectively, from 7 mice, bootstrap, $p > 0.05$.
Figure S4U. REM- versus REM+: pre-shock HC, n = 13 and 11 events, $p = 0.47$, bootstrap; pre-shock A, n = 22 and 17 events, $p = 0.50$, bootstrap; post-shock A, n = 16 and 20 events, $p = 0.87$, bootstrap; test A, n = 15 and 9 events, bootstrap, $p = 0.12$.
Figure S5C. BL, n = 548 neurons; AS, n = 361 neurons from 6 mice; REM: AS versus BL, bootstrap, $p > 0.05$.
Figure S5H. n = 7 neurons from 2 mice, two-tailed paired t test, $t(5) = 29.9$, $p < 0.0001$.
Figure S5I. n = 7 neurons from 2 mice, two-tailed Wilcoxon matched-pairs signed rank test, $p < 0.05$.
Figures S5K–S5M. DS/-/Halo (AAV:pCaMKII-Cre:Halo mice in the DS group without light delivery), 1704 spines, n = 32 dendrites, 14 neurons, 3 mice. DS/+/Halo (AAV:pCaMKII-Cre:Halo mice in the DS group with orange light delivery), 1783 spines, n = 34 dendrites, 18 neurons, 4 mice. (K) Two-tailed unpaired t test, $t(64) = 0.000084$, $p = 1.0$. (L) Two-tailed unpaired t test, $t(64) = 0.73$, $p = 0.47$. (M) Two-tailed unpaired t test, $t(64) = 0.37$, $p = 0.71$.
Figure S5O. n = 13 mice/group, Kruskal-Wallis test, $p = 0.16$

Inventory of Supplemental Information

Figure S1 shows evidence of successful transgene induction in ABNs from pNestinCreER^{T2} mice, related to Figures 1, 2, 3, 4, 5, and 6.
Figure S2 shows that ∼4 week-old ABNs made connections with medial temporal neuronal circuitry, related to Figures 1, 2, 3, 4, 5, and 6.
Figure S3 explains how we defined Ca^{2+} transients from video recordings, estimated their rate using bootstrap methods, and longitudinally tracked the same neurons, related to Figure 1
Figure S4 shows detailed data from Ca^{2+} imaging experiments, related to Figure 1.
Figure S5 provides control data from granular neurons, related to Figures 1, 2, 5, and 6.
Figure S6 shows placement of optic cannulas, related to Figures 1, 3, 4, 5, and 6.
Video S1 is an example Ca^{2+} recording video, related to Figure 1.
Video S2 is an example EEG and EMG recording video, related to Figures 1, 3, 4, 5, and 6.
Table S1 shows evidence of successful light delivery in each vigilance stage, related to Figures 1, 3, 4, 5, and 6.
Data S1 provides detailed results of statistical analyses, related to Figures 3D–3F.
Data S2 provides detailed results of transcriptome analysis, related to Figure 4.